Pattern formation in the presence of symmetries

Gemunu H. Gunaratne*
Department of Physics, The University of Houston, Houston, Texas 77204

Qi Ouyang† and Harry L. Swinney‡
Center for Nonlinear Dynamics and Department of Physics, The University of Texas, Austin, Texas 78712

(Received 24 March 1994)

We present a detailed theoretical study of pattern formation in planar continua with translational, rotational, and reflection symmetry. The theoretical predictions are tested in experiments on a quasi-two-dimensional reaction-diffusion system. Spatial patterns form in a chlorite-iodide-malonic acid reaction in a thin gel layer reactor that is sandwiched between two continuously refreshed reservoirs of reagents; thus, the system can be maintained indefinitely in a well-defined nonequilibrium state. This physical system satisfies, to a very good approximation, the Euclidean symmetries assumed in the theory. The theoretical analysis, developed in the amplitude equation formalism, is a spatio-temporal extension of the normal form. The analysis is identical to the Newell-Whitehead-Segel theory [J. Fluid Mech. **38**, 203 (1969); **38**, 279 (1969)] at the lowest order in perturbation, but has the advantage that it exactly preserves the Euclidean symmetries of the physical system. Our equations can be derived by a suitable modification of the perturbation expansion, as shown for two variations of the Swift-Hohenberg equation [Phys. Rev. A **15**, 319 (1977)]. Our analysis is complementary to the Cross-Newell approach [Physica D **10**, 299 (1984)] to the study of pattern formation and is equivalent to it in the common domain of applicability. Our analysis yields a rotationally invariant generalization of the phase equation of Pomeau and Manneville [J. Phys. Lett. **40**, L609 (1979)]. The theory predicts the existence of stable rhombic arrays with qualitative details that should be system independent. Our experiments in the reaction-diffusion system yield patterns in good accord with the predictions. Finally, we consider consequences of resonances between the basic modes of a hexagonal pattern and compare the results of the analysis with experiments.

PACS number(s): 47.54.+r, 82.40.Ck, 82.20.Wt, 47.20.Ky

I. INTRODUCTION

A. Prologue

There is a striking similarity in a bewildering array of natural patterns ranging from cloud streets and patterns in sand dunes to animal coats, fish scales, and beehives. The patterns are often regular on a small scale (typically consisting of stripes or hexagons) but form highly complex structures on a large scale. The commonality of patterns generated in disparate systems demands a study that transcends the microscopic details of the physical system. Such an analysis of patterns should address several questions. Why do pattern forming systems exhibit only a few distinct structures on a small scale? What are these possible "local" structures, and what determines the "small" scale? Can the universality be traced back to some general features of the pattern genesis and evolution? What is the origin of the irregularity and nonuniversality of patterns on a large scale? What roles do thermal noise, boundaries, initial conditions, and dissipation play in pattern formation?

A wide array of controlled experimental systems, including chemical reactions [1], Rayleigh-Bénard convection [2], ferrofluids [3], and magnetic bubble material [4], have been used to study pattern formation. Figure 1 shows some patterns we have obtained in experiments on a reaction-diffusion system. The spontaneous formation of spatial patterns in chemical systems was first predicted in 1952 by Alan Turing [5] in a classic paper entitled "On the chemical basis for morphogenesis." However, despite much effort, Turing patterns were not observed in controlled laboratory experiments until recently [6–8], following the development of a laboratory reactor in which reaction and diffusion processes can be sustained while at the same time advection is inhibited using an inert gel [9,10].

The amplitude equation formalism introduced by Newell, Whitehead, and Segel [11] is a natural scheme to extract universal properties of pattern formation. However, this spatiotemporal extension of the normal form theory lacks rotational invariance, which is crucial for an analysis of patterns such as those of Fig. 1. We take an alternative approach, demanding that the spatio-temporal extension satisfy the rotational invariance *ex-*

*Electronic address: gemunu@uh.edu
†Electronic address: qi@chaos.utexas.edu
‡Electronic address: swinney@chaos.utexas.edu

actly. The resulting model is identical to the Newell-Whitehead-Segel theory at the lowest order, but respects the Euclidean symmetries of the physical system. In certain limits our model can be generated systematically by "regularizing" the multiple scale perturbation theory of Newell-Whitehead-Segel so that the symmetry of the underlying system is enforced. In the spirit of the normal form theory, we compare the *qualitative* behavior of the model (e.g., the stability of local structures, bifurcations between states) to the experiments even beyond the range of validity of the perturbation expansion.

B. Overview of the paper

Patterns can form via distinct mechanisms such as symmetry breaking [12] and interaction between kinks [13,14]. Spontaneous symmetry breaking leads to states with less symmetry than the physical system, i.e., patterns. The systems we consider are invariant under Euclidean motions in the plane: translations, rotations, and reflections. The constraints imposed by the symmetries, together with the assumption of continuity, restrict the possible structures generated. While our study is restricted to systems that show pattern competition between hexagons and stripes, the approach is easily extended to squares and other planforms [15].

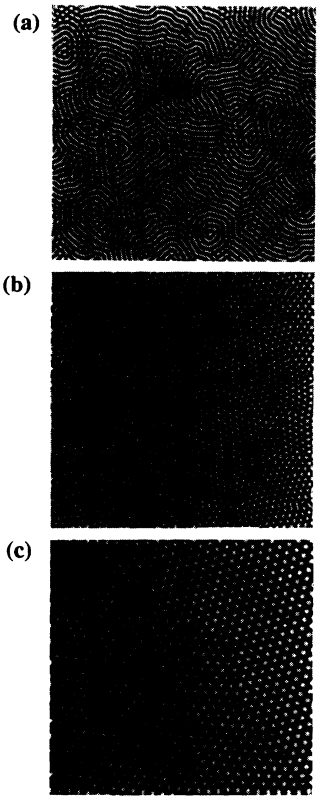

FIG. 1. Chemical patterns observed in a quasi-two-dimensional reaction-diffusion system with the chlorite-iodide-malonic acid reaction: (a) multiple domains of stripes, (b) multiple domains of hexagons of different orientations, and (c) a pattern with a single grain boundary separating hexagonal lattices with different orientations. The reaction occurs in a thin polyvinyl alcohol layer contained between two reservoirs. The wavelength of the patterns are (a) 0.11 mm, (b) 0.12 mm, and (c) 0.18 mm. The region shown is a 6 mm × 6 mm section of the 25 mm diam reactor. The malonic acid concentrations in reservoir B were (see Fig. 3) (a) 27 mM, (b) 24 mM, and (c) 32 mM. Other control parameters were held fixed at $[I^-]_0^{A,B} = 2.2$ mM, $[Na_2SO_4]_0^{A,B} = 4.5$ mM, $[ClO_2^-]_0^A = 22$ mM, $[H_2SO_4]_0^A = 1$ mM, $[H_2SO_4]_0^B = 20$ mM, and temperature 7.0 °C.

Several predictions made on the basis of the theory are supported by our experiments on a reaction-diffusion system involving chlorite ions, iodide ions, and malonic acid (the "CIMA" reaction [16]) [17]. The reaction occurs in a thin gel layer contained between two continuously fed well-stirred (homogeneous) reactors. For some values of the control parameters (i.e., the reagent concentrations and reactor temperature), the chemical concentrations are constant in any plane of the thin gel layer—there is no pattern—while for other control parameter values, patterns spontaneously emerge and are stable, as illustrated in Fig. 1. The details of the reactor and measurement systems will be described in Sec. IV.

Our analysis is not restricted to chemical patterns. Accordingly, let $U(\mathbf{x},t)$ denote the intensity of any scalar field that characterizes a two-dimensional pattern. For the CIMA reaction, $U(\mathbf{x},t)$ could denote the difference between the local concentration and the mean value of the triiodide complex formed in the reaction. For surface-tension driven convection, $U(\mathbf{x},t)$ could represent the fluid surface temperature or a component of the fluid surface velocity. Prior to the bifurcation, the uniform solution $U(\mathbf{x},t) = 0$ is stable against all perturbations. The primary bifurcation results in the loss of translational invariance and typically leads to patterns with a characteristic length scale.

The planform that lends itself to the most elementary analysis is a periodic array of stripes. This essentially one-dimensional pattern (there being no variation along the the axis of the stripes) can be expanded in a Fourier series

$$U(\mathbf{x},t) = Ae^{i\mathbf{k}\cdot\mathbf{x}} + \text{c.c.}, \tag{1.1}$$

where A is the *amplitude* of the stripes; the magnitude of $\mathbf{k}$, k_0, is determined by the characteristic length scale of the pattern. The addition of the complex conjugate c.c. allows the field $U(\mathbf{x},t)$ to be real.

The stability and dynamics of an array of stripes can be determined via the *normal form equation* [18] for the dynamics of the amplitude $A(t)$,

$$\dot{A} = f(A) = \mu A - |A|^2 A, \tag{1.2}$$

where $\dot{A}$ denotes the time derivative and, as we argue in Sec. II, the parameter μ needs to be real to reflect the invariances of the physical system. The theory describes bifurcations between the uniform state and a periodic array of stripes. Unfortunately, the normal form theory can be applied to extended structures (via Liapunov-Schmidt reduction) only when the pattern is exactly periodic [19].

How can this theory can be generalized to study patterns that are slowly varying, i.e., patterns that are striped on a small scale but have a more complex structure on a large scale, as in Fig. 1(a)? Such an extension has been developed by Newell, Whitehead, and Segel for the expansion (1.1) [11], although it has not yet been made rigorous.

The Newell-Whitehead-Segel theory is based on the observation that close to the onset of patterns, the uniform state is unstable only to perturbations with wave vectors close to k_0. Consequently, the corrections to the expansion [of, say, (1.1)] are *slowly varying* with respect to the basic length scale $(2\pi/k_0)$. The theory is developed as a perturbation series in the inverse of this scale by allowing *slow* spatial variations in $A \equiv A(\mathbf{x},t)$. If $\mathbf{k}$ is chosen along the x direction, the resulting *multiple scale analysis* gives for the dynamics of the envelope function $A(\mathbf{x},t)$:

$$\partial_t A(\mathbf{x},t) = \mu A - |A|^2 A + \left(\partial_x - \frac{i}{2k_0}\partial_{yy}\right)^2 A, \quad (1.3)$$

which is often referred to as a Landau-Ginzburg equation. This generalization of the normal form (1.2) gives a clear description of the instabilities of an array of rolls in Rayleigh-Bénard convection [20]. More importantly, Eq. (1.3) is independent of the underlying microscopic equations and depends only on general features of the system; thus it describes universal properties of an array of stripes [12]. However, the approach can be applied only to an array of stripes pointing in a given direction *everywhere in space*. According to Eq. (1.3), the behavior of an array of stripes pointing in another direction will be different. This is unacceptable for a physical system that is invariant under rotations. In rotationally invariant systems two patterns related by rotation (or the action of any of the symmetries) have to evolve the same way. Equations of motion that allow such dynamics are termed *equivariant* [19].

We illustrate, through an example, the need for amplitude equations to be equivariant under the symmetries of the physical system. Consider a boundary (say, $x = 0$) separating two semi-infinite domains of uniform stripes and let the stripes make the same angle with the boundary separating the domains. Since the original physical system is symmetric under rotations, there can be no transverse motion of the domain wall. However, with nonequivariant Landau-Ginzburg equations, different domains will in general have different stabilities and consequently there can be a transverse motion of the domain wall. This simple argument illustrates the need for the amplitude equations to be equivariant under the symmetries of the physical system.

In Sec. II we take a different approach, demanding that the spatiotemporal extension of the normal form be equivariant under rotations. The restriction implies that spatial derivatives acting on the envelope functions $A(\mathbf{x},t)$ should appear in the combination

$$\Box = \left(\hat{\mathbf{k}}\cdot\boldsymbol{\nabla} - \frac{i}{2k_0}\nabla^2\right), \quad (1.4)$$

where $\hat{\mathbf{k}}$ is the unit vector $\mathbf{k}/k_0$ and $\boldsymbol{\nabla}$ is in the two-dimensional plane of the pattern. Equation (1.3) will thus be replaced by

$$\partial_t A(\mathbf{x},t) = \mu A - |A|^2 A + \Box^2 A, \quad (1.5)$$

which is equivariant under rotations, reflections, and translations.

In Sec. III we present a variation of the multiple scale analysis of Newell-Whitehead-Segel that leads to equivariant amplitude equations. We argue that the multiple scale analysis leads to loss of symmetries only when the expansion is truncated at a finite stage. When the perturbation is carried out to higher order, each term is "symmetrized" to a form that leads to equivariant dynamics. Thus the term $(\partial_x - \frac{i}{2k_0}\partial_{yy})^2 A(\mathbf{x},t)$ of Eq. (1.3) appearing at the lowest order in perturbation (of, for example, the Swift-Hohenberg equation [21]) is symmetrized to $\Box^2 A(\mathbf{x},t)$ when the perturbation is carried out to higher order. In Appendix A we derive the amplitude equations in a hexagonal basis and show how several terms that appear in the amplitude equations are symmetrized, leading to equivariant dynamics.

The scheme described above "regularizes" the multiple scale expansion so that the symmetries lost in the truncation of the multiple scale analysis are restored. The imposition of physical features of a system in selection of terms of a perturbation series has also been essential in some analyses of Hamiltonian systems [22] and random phase approximations [23]. Given that neither Eq. (1.5) nor Eq. (1.3) has the rigorous theoretical foundation of the normal form theory, we see no advantage of retaining terms up to a given order in perturbation at the cost of losing the symmetries of the physical system. The equivariance of Eq. (1.5) under Euclidean symmetries is a significant advantage we get through the new scheme. Equation (1.3) describes properties of physical systems that do not posses rotational invariance, while Eq. (1.5) models spontaneous symmetry breaking, i.e., it describes patterns generated in physical systems with Euclidean symmetries.

Even though Eq. (1.5) was derived via the multiple scale analysis, we will use it as a model in its own right. In particular, the competition between stripes and hexagons will be examined well beyond the range of validity of the perturbation analysis. Thus we have less reason to retain a given order in perturbation at the risk of losing the equivariance that preserves the symmetries of the physical system.

The amplitude equations derived in Sec. II admit linearly stable solutions that correspond to periodic rhombic arrays. Distortion of a hexagonal array (mediated by diffusion) leads to these rhombic arrays. The rhombic arrays are generated in systems that have the Euclidean symmetries and show several novel features. They occur for a band of characteristic angles and can point in arbitrary directions. Thus a random initial state will generally evolve into a pattern of multiple domains, each with its own direction and characteristic angle. Figures 1(b) and 1(c) are examples of such states. Several universal features of the rhombic arrays, derived in Sec. V

from the theory of Sec. II, have been confirmed in the chemical patterns. The theory, which is based only on the symmetries and continuity, suggests that rhombic arrays should be observed in other continuum interfaces, e.g., Marangoni convection, driven surface waves (Faraday crispations), magnetic bubbles, and flame fronts.

Far beyond the onset of patterns, the resonances between the basic modes of a hexagonal array can lead to secondary modes, which introduce a nontrivial structure into the building blocks of the hexagonal array [24]. In Sec. VI we present experimental observations of these states, which we refer to as "black-eye" patterns (see Fig. 8 for example). We describe the transitions to and from the "black eyes" observed in the CIMA reaction. In Appendix A we show explicitly how the resonant terms appear in the multiple scale expansion of the Swift-Hohenberg equation.

As we have already indicated, the rotational invariance of the model is crucial in studying the dynamics of domain walls. In Sec. VII we examine the behavior of domain walls between striped regions of different orientations. Numerical simulations indicate qualitative differences in the form of boundaries generated by amplitude equations that contain the proper symmetries and those that lack these symmetries. We also consider the numerical evolution of a pattern with multiple domains of hexagons and stripes, and we show that regions of hexagons and stripes invade each other over long periods (compared to the diffusion time) before one pattern dominates. Similar behavior is found in patterns formed in the experiments on the CIMA reaction.

Finally, we study patterns resulting from the numerical integration of our model, starting from random initial states. Qualitative differences are found for structures generated from variational and nonvariational dynamics. In the variational case the patterns stabilize and uniform arrays of stripes on either side of a domain wall tend to make an angle close to 60° with the boundary. This is reminiscent of patterns generated in ferrofluids [3] and magnetic bubble material [4]. Conversely, when the dynamics is nonvariational the patterns do not appear to settle down and arrays of uniform stripes have less well defined boundaries. Structures that develop in the CIMA reaction [1] and Rayleigh-Bénard convection [2] are qualitatively similar to the nonvariational patterns in the simulation.

In Sec. VIII we discuss some unique features of our approach to amplitude equations. In particular we note that the amplitude equations can be generated by insisting only on the equivariance under the Euclidean symmetries. Perhaps this approach will lead to a rigorous basis for the Landau-Ginzburg equations. Our predictions on patterns can be checked in other experiments. In particular, it will be extremely interesting to see if, nearly a century after Bénard's discovery of hexagons and Rayleigh's prediction of convection rolls, another type of periodic array (i.e., rhombic array) will be observed in fluid convection.

Appendix A describes a multiple scale analysis of two variants of the Swift-Hohenberg equation in the hexagonal basis. In particular, it is shown how terms that make the amplitude equations nonequivariant at low order in the expansion are symmetrized on carrying out the perturbation to higher order. These calculations make it clear why the truncated expansions can be regulated by carrying out the perturbation expansion to higher order.

A rotationally invariant theory for the study of pattern formation has been developed previously by Cross and Newell [25], who analyze patterns that are locally roll-like almost everywhere in space. Our amplitude equations are complementary to theirs in the following sense. The Cross-Newell equations are valid for a larger range of parameters (from the onset of patterns), but are limited to the study of slowly varying stripes. Our amplitude equations are valid only close to the onset of patterns but can be used to study more general structures, e.g., an array of slowly varying hexagons or a complex pattern consisting of stripes and hexagons. In Appendix B it is shown that the theories are equivalent in the parameter domain where both are valid. The analysis also yields a rotationally invariant generalization of the phase equation of Pomeau and Manneville [26].

II. SYMMETRY AND THE LANDAU-GINZBURG EQUATIONS

In this section we deduce the form of the equivariant amplitude equations through an analysis of the symmetries. Uniform planar periodic patterns most often seen in experimental and natural systems are hexagons and stripes. A scalar field $U(\mathbf{x},t)$ that characterizes them can be expanded in a *hexagonal planform* as [12]

$$U(\mathbf{x},t) = A_1 e^{i\mathbf{k}_1\cdot\mathbf{x}} + A_2 e^{i\mathbf{k}_2\cdot\mathbf{x}} + A_3 e^{i\mathbf{k}_3\cdot\mathbf{x}} + \text{c.c.}, \quad (2.1)$$

where $\mathbf{k}_n$ are a set of hexagonal basis vectors, e.g.,

$$\mathbf{k}_1 = k_0\mathbf{j}; \mathbf{k}_2 = k_0\left(\frac{\sqrt{3}}{2}\mathbf{i} - \frac{1}{2}\mathbf{j}\right), \quad (2.2)$$

$$\mathbf{k}_3 = k_0\left(-\frac{\sqrt{3}}{2}\mathbf{i} - \frac{1}{2}\mathbf{j}\right).$$

The envelope functions for a uniform array of stripes parallel to the x axis are $A_1 \neq 0$ and $A_2 = A_3 = 0$, while those for a uniform array of hexagons satisfy $A_1 = A_2 = A_3$. In the hexagonal basis, the normal form equations for the dynamics of $A_n(t)$ are [27,28]

$$\begin{aligned}
\dot{A}_1 = f_1(t) &= \mu A_1 + \alpha\bar{A}_2\bar{A}_3 \\
&\quad -(|A_1|^2 + \rho|A_2|^2 + \rho|A_3|^2)A_1, \\
\dot{A}_2 = f_2(t) &= \mu A_2 + \alpha\bar{A}_3\bar{A}_1 \\
&\quad -(|A_2|^2 + \rho|A_3|^2 + \rho|A_1|^2)A_2, \\
\dot{A}_3 = f_3(t) &= \mu A_3 + \alpha\bar{A}_1\bar{A}_2 \\
&\quad -(|A_3|^2 + \rho|A_1|^2 + \rho|A_2|^2)A_3,
\end{aligned} \quad (2.3)$$

where $\dot{A}$ and $\bar{A}$ denote the time derivative and the complex conjugate of A, respectively, and, as we argue below,

parameters μ, α, and ρ need to be real to reflect the invariances of the physical system.

The normal form expansion (2.3) allows us to study the existence and stability of arrays of hexagons and stripes, as well as bifurcations between these and the uniform state. Equations (2.3) are based only on the symmetries of the interface and thus describe common features of patterns generated in a large class of two-dimensional continua. Since $\mathbf{k}_1$, $\mathbf{k}_2$, and $\mathbf{k}_3$ can be permuted in (2.1), Eqs. (2.3) are invariant under any permutation of indices. The reflection symmetry of the physical system requires that the equations of motion be equivariant under reflections, i.e., given a pattern $U(\mathbf{x}, t_0)$, the evolution of the pattern reflected about the y axis, $V(\mathbf{x}, t_0) = U(\kappa^{-1}\mathbf{x}, t_0)$ (with envelope functions A_1, A_3, and A_2), has to satisfy $V(\mathbf{x}, t) = U(\kappa^{-1}\mathbf{x}, t)$ for $t > t_0$. This is obviously true for (2.3). The need for Eq. (2.3) to be equivariant under reflections about the x axis requires $(\bar{A}_1, \bar{A}_2, \bar{A}_3)$ to be a solution and restricts μ, α, and ρ to be real. Finally, equivariance under a translation $\mathbf{x}_0$ implies that $A_n e^{-i\mathbf{k}_n\cdot\mathbf{x}_0}$ $(n = 1, 2, 3)$ are a set of solutions of Eq. (2.3) and determines the form of the allowed nonlinear coupling terms (e.g, the terms $\bar{A}_2\bar{A}_3$ and $|A_2|^2 A_1$ in the first equation).

Figure 2 summarizes the linear stabilities of the uniform state and arrays of hexagons and stripes. In this model, hexagons appear through a subcritical bifurcation while (unstable) stripes are created via a supercritical bifurcation. Mixed states (which correspond to $A_2 = A_3 \neq A_1$) can exist, but are unstable in the model [28].

The normal form (2.3) can be used only to describe arrays of hexagons or stripes that are exactly periodic, while most experimental patterns consist of local periodic patches that are arranged in a complex mosaic on a large scale, as Fig. 1 illustrates. External noise and inhomogeneity of the initial state can lead to the complexity of these patterns. The patterns also show *defects*—points at which the direction of the rolls is not defined uniquely. The existence of qualitatively similar patterns in experiments [1–4], mathematical models [12,29,30], and nature demands a model-independent description of pattern formation.

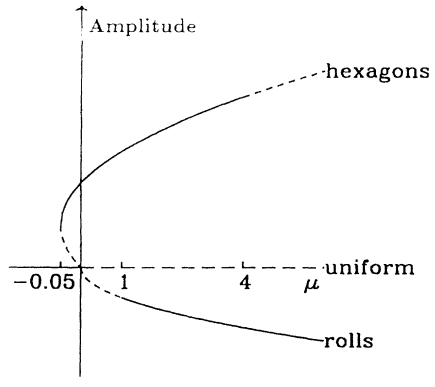

FIG. 2. The stability domains of the uniform state, hexagons, and stripes in the normal form equations (2.3). Solid lines correspond to stable states while dashed lines correspond to unstable states. The parameters α and ρ are chosen to be 1 and 2, respectively. The negative direction of the x axis has been stretched for clarity.

The normal form can be generalized to describe slowly varying structures with envelope functions $A_n(\mathbf{x}, t)$ by the addition of suitable spatial derivatives. The form of the spatial derivatives can be determined by requiring the resulting equations to be equivariant under *arbitrary* rotations. The action of a rotation $\mathcal{R}$ on a pattern $U(\mathbf{x}, t)$ leads to a second pattern $V(\mathbf{x}, t) = U(\mathcal{R}^{-1}\mathbf{x}, t)$, and we require $V(\mathbf{x}, t)$ to be a solution of our amplitude equations. The required condition can be deduced by analyzing a uniform array of stripes. Stripes parallel to the x axis are given by $U_0 = a_1 e^{i\mathbf{k}_1\cdot\mathbf{x}}$, while those oriented at an angle θ to the x axis can be written as $U_\theta = a_1 e^{i\mathbf{k}_1(\theta)\cdot\mathbf{x}}$, with $\mathbf{k}_1(\theta) = (k_0 \sin\theta)\mathbf{i} + (k_0 \cos\theta)\mathbf{j}$. Rotational invariance implies that a_1 is independent of θ. The solution U_θ can be expanded in the original basis $(\mathbf{k}_1, \mathbf{k}_2, \mathbf{k}_3)$ using envelope functions

$$A_1 = a_1 e^{i\Delta\mathbf{k}_1\cdot\mathbf{x}} \quad , \quad A_2 = A_3 = 0, \tag{2.4}$$

with $\Delta\mathbf{k}_1 = \mathbf{k}_1(\theta) - \mathbf{k}_1 = k_0 \sin\theta\mathbf{i} - k_0(1 - \cos\theta)\mathbf{j}$. What is needed then is a combination $\Box_1$ of spatial derivatives that will satisfy the condition $\Box_1 e^{i\Delta\mathbf{k}_1\cdot\mathbf{x}} = 0$. It is easy to check that

$$\Box_1 = \left(\hat{\mathbf{k}}_1 \cdot \boldsymbol{\nabla} - \frac{i}{2k_0}\nabla^2\right) \tag{2.5}$$

is the simplest such combination. Defining $\Delta\mathbf{k}_2$, $\Delta\mathbf{k}_3$, $\Box_2$, and $\Box_3$ analogously, we see, as a consequence of the invariance of $(\sin^2\theta + \cos^2\theta)$, that

$$\Box_n e^{i\Delta\mathbf{k}_n\cdot\mathbf{x}} = 0 \tag{2.6}$$

for $n = 1, 2, 3$. We are thus motivated to introduce an extension of the normal form equations

$$\partial_t A_1 = f_1(\mathbf{x}, t) + \gamma\,\Box_1^2\, A_1 + \nu\bar{\Box}_2\bar{A}_2\bar{\Box}_3\bar{A}_3, \tag{2.7a}$$

$$\partial_t A_2 = f_2(\mathbf{x}, t) + \gamma\,\Box_2^2\, A_2 + \nu\bar{\Box}_3\bar{A}_3\bar{\Box}_1\bar{A}_1, \tag{2.7b}$$

$$\partial_t A_3 = f_3(\mathbf{x}, t) + \gamma\,\Box_3^2\, A_3 + \nu\bar{\Box}_1\bar{A}_1\bar{\Box}_2\bar{A}_2 \tag{2.7c}$$

to describe the dynamics of the spatially dependent envelope functions $A_n(\mathbf{x}, t)$. Here $f_n(\mathbf{x}, t)$ is the spatiotemporal extension of $f_n(t)$ defined in (2.3) and $\bar{\Box}_n$ is the complex conjugate of $\Box_n$.

Some comments are in order. First, given a pattern $U(\mathbf{x}, t)$, the envelope functions for the rotated pattern $U(\mathcal{R}^{-1}\mathbf{x}, t)$ are $A'_n = A_n(\mathcal{R}^{-1}\mathbf{x}, t)e^{i\Delta\mathbf{k}_n\cdot\mathbf{x}}$ [31]. It follows from (2.6) that A'_n are solutions of (2.7) and hence the amplitude equations are equivariant under *arbitrary* rotations, as was required all along. Second, observe that when $\nu = 0$, (2.7) can be derived from a variational principle, $\partial_t A_k = -\delta(\int dxdy\mathcal{L})/\delta\bar{A}_k$ with

$$\mathcal{L} = -\mu \sum_{n=1}^{3} |A_n|^2 - \alpha(A_1 A_2 A_3 + \bar{A}_1 \bar{A}_2 \bar{A}_3) + \frac{1}{2} \sum_{n=1}^{3} |A_n|^4 + \rho \sum_{n \neq m} |A_n|^2 |A_m|^2 + \gamma \sum_{n=1}^{3} |\Box_n A_n|^2. \quad (2.8)$$

Thus the last terms in (2.7) are required to capture nonvariational effects on pattern formation. Finally, several other combinations of spatial derivatives could have been added to (2.7) without violating the symmetries. The terms $\Box_n^2 A_n$ were introduced to model effects of diffusion while terms such as $\bar{\Box}_2 \bar{A}_2 \bar{\Box}_3 \bar{A}_3 \ldots$ were added to model nonvariational effects. Terms such as $i \Box_1 A_1$ and $i(\bar{A}_2 \bar{\Box}_3 \bar{A}_3 + \bar{A}_3 \bar{\Box}_2 \bar{A}_2)$ can be added to the first of Eqs. (2.7) (with corresponding terms in the other equations) without violating the symmetries. However, they can be scaled away (individually) by suitable redefinitions of k_0 and thus cannot lead to *qualitatively* different behavior. In Appendix A we give some other combinations of spatial derivatives that lead to equations of motion that are equivariant under the Euclidean symmetries.

Equations similar in form to (2.7), but with $\Box_n$ approximated by $(\hat{\mathbf{k}}_n \cdot \boldsymbol{\nabla})$, have been introduced in Ref. [32]. Qualitative properties of uniform states such as the stability of hexagons, and stripes and the existence of rhombic arrays will be identical in both models. However, there will be significant differences in the two models that can be traced back to the absence of equivariance in the model in Ref. [32]. For example, even though periodic arrays of stripes, hexagons and rhombi are solutions of the nonequivariant equations, they cannot be oriented in arbitrary directions. In contrast, any solution of (2.7) and a second solution related by rigid body symmetries have identical stability properties. As mentioned in Sec. I, the rotationally invariant formulation will be crucial in the study of domain walls between stripes pointing in different directions (see Sec. VII).

Finally, use of the rotationally invariant formulation has a significant advantage in the numerical integration of amplitude equations. If Eq. (1.3) or a nonequivariant extension of (2.3) is used to study the dynamics of a spatially slowly varying array of stripes or hexagons, one has to define a local basis in each neighborhood (with the two axes pointing parallel and normal to the local stripes) and study the dynamics via envelope functions defined in this basis. When the stripes evolve in time, the local axes have to be changed along with the direction of the stripes. This is obviously not a practical scheme to study the dynamics of patterns. With the rotationally invariant formulation one can define a global set of axes and study the dynamics of the envelope functions for all times.

III. MULTIPLE SCALE ANALYSIS

The amplitude equations (1.5) and (2.7) for the dynamics of the envelope functions $A_n(\mathbf{x}, t)$ were deduced on the basis of symmetries. In this section we introduce a modification of the multiple scale analysis of Newell-Whitehead-Segel that leads to equivariant amplitude equations. Specifically, we regularize the truncated perturbation expansion by enforcing the required invariances by symmetrizing each term of the amplitude equations. As shown below, the symmetrized form of each term is deduced by carrying out the multiple scale analysis to higher order. For example, the lowest order in perturbation of the Swift-Hohenberg equation via (1.1) gives spatial derivatives in a combination $(\hat{\mathbf{k}} \cdot \nabla)^2 A(\mathbf{x}, t)$. The resulting equations are not equivariant and can be made so by symmetrizing the term to $\Box^2 A(\mathbf{x}, t)$. In this section and Appendix A, we show how several terms used in Landau-Ginzburg equations are symmetrized to give dynamics that respect the Euclidean symmetries.

For clarity and simplicity, we limit our calculations to a generalization of the Swift-Hohenberg equation [21]

$$\partial_t U(\mathbf{x}, t) = [\epsilon^2 - (1 + \nabla^2)^2] U(\mathbf{x}, t) - \gamma [U(\mathbf{x}, t)]^3 + \epsilon \beta U(\mathbf{x}, t) \nabla^2 U(\mathbf{x}, t). \quad (3.1)$$

The last term makes the equation nonvariational and breaks the $U \to -U$ symmetry. In Appendix A we provide the results of the multiple scale expansion of a second generalization of the Swift-Hohenberg equation,

$$\partial_t U(\mathbf{x}, t) = [\epsilon^2 - (1 + \nabla^2)^2] U(\mathbf{x}, t) - \gamma [U(\mathbf{x}, t)]^3 + \epsilon \beta [\boldsymbol{\nabla} U(\mathbf{x}, t)]^2. \quad (3.2)$$

The nonvariational term here is the nonlinear term of the Kuramoto-Sivashinsky equation [33].

The seminal work of Newell-Whitehead-Segel is built on the observation that, close to the onset of patterns, the uniform state is unstable only to perturbations with wave vectors close to k_0. Consequently, variations in $A_n(\mathbf{x}, t)$ occur on a scale much larger than the basic scale $(2\pi/k_0)$ and $A_n(\mathbf{x}, t)$ can be written in terms of the *slow* variables

$$X = \epsilon x \quad , \quad Y = \epsilon y \quad , \quad T = \epsilon^2 t. \quad (3.3)$$

Unlike the original scaling introduced by Newell-Whitehead-Segel, we scale the x and y directions by the same factor. This is equivalent to having the basic striped state *not* be parallel to either coordinate axis. The quadratic maximum of the dispersion relation is reflected in the scaling of t by ϵ^2 [12,34]. Following the standard notation, we can write the spatial and temporal derivatives as

$$\boldsymbol{\nabla} \to \boldsymbol{\nabla}_0 + \epsilon \tilde{\boldsymbol{\nabla}}, \qquad \partial_t \to \epsilon^2 \partial_T, \quad (3.4)$$

where $\boldsymbol{\nabla}_0 = (\mathbf{i}\partial_x + \mathbf{j}\partial_y)$ operates on the "fast" variations $e^{\mathbf{i}\mathbf{k}\cdot\mathbf{x}}$ and $\tilde{\boldsymbol{\nabla}} = (\mathbf{i}\partial_X + \mathbf{j}\partial_Y)$ acts on the slowly varying envelope functions. The operator $(1 + \nabla^2)^2$ is replaced by

$$(1 + \nabla^2)^2 \to \mathcal{L}_0 + \epsilon \mathcal{L}_1 + \epsilon^2 \mathcal{L}_2 + \epsilon^3 \mathcal{L}_3 + \epsilon^4 \mathcal{L}_4, \quad (3.5)$$

with

$$\begin{aligned}
\mathcal{L}_0 &= (1+\nabla_0^2)^2,\\
\mathcal{L}_1 &= 4(1+\nabla_0^2)(\boldsymbol{\nabla}_0\cdot\tilde{\boldsymbol{\nabla}}),\\
\mathcal{L}_2 &= 2(1+\nabla_0^2)\tilde{\nabla}^2+4(\boldsymbol{\nabla}_0\cdot\tilde{\boldsymbol{\nabla}})^2,\\
\mathcal{L}_3 &= 4\tilde{\nabla}^2(\boldsymbol{\nabla}_0\cdot\tilde{\boldsymbol{\nabla}}),\\
\mathcal{L}_4 &= \tilde{\boldsymbol{\nabla}}^4.
\end{aligned} \tag{3.6}$$

We expand the field $U(\mathbf{x},t)$ as

$$U(\mathbf{x},t)=\epsilon w_1(\mathbf{x},t)+\epsilon^2 w_2(\mathbf{x},t)+\epsilon^3 w_3(\mathbf{x},t)+\cdots. \tag{3.7}$$

The expansions of nonlinear terms U^3 and $U\nabla^2 U$ in ϵ are

$$\begin{aligned}
U(\mathbf{x},t)^3 &= \epsilon^3 w_1^3+3\epsilon^4 w_1^2 w_2\\
&\quad +3\epsilon^5(w_1^2 w_3+w_1 w_2^2)+O(\epsilon^6)
\end{aligned} \tag{3.8}$$

and

$$\begin{aligned}
U\nabla^2 U &= \epsilon^2 w_1\nabla_0^2 w_1\\
&\quad +\epsilon^3[w_2\nabla_0^2 w_1+2w_1(\boldsymbol{\nabla}_0\cdot\tilde{\boldsymbol{\nabla}})w_1+w_1\nabla_0^2 w_2]\\
&\quad +\epsilon^4[\nabla_0^2(w_1 w_3)+2\boldsymbol{\nabla}_0\cdot\tilde{\boldsymbol{\nabla}}(w_1 w_2)\\
&\quad +w_2\nabla_0^2 w_2+w_1\tilde{\nabla}^2 w_1]+O(\epsilon^5).
\end{aligned} \tag{3.9}$$

Using the scaling (3.3)–(3.9), we can expand (3.1) in a perturbation series in ϵ. At order ϵ^1, we get $\mathcal{L}_0 w_1=0$, which implies

$$w_1(\mathbf{x},t)=A_{11}(\mathbf{X},T)e^{i\mathbf{k}\cdot\mathbf{x}}+\text{c.c.}, \tag{3.10}$$

c.c. denoting the complex conjugate, and $|\mathbf{k}|=1$. [We use the notation in Ref. [35]. Thus A_{mn} is the coefficient of $e^{ni\mathbf{k}\cdot\mathbf{x}}$ in a Fourier expansion of $w_m(\mathbf{x},t)$.] At order ϵ^2 in the expansion, we get $\mathcal{L}_0 w_2+\mathcal{L}_1 w_1=0$, which gives

$$w_2(\mathbf{x},t)=A_{21}(\mathbf{X},T)e^{i\mathbf{k}\cdot\mathbf{x}}+\text{c.c.} \tag{3.11}$$

Both w_1 and w_2 are expanded in the same direction $\mathbf{k}$ because we wish to study modulations of a (locally) periodic array of stripes. At the third order in the expansion we get

$$\mathcal{L}_0 w_3=-\partial_T w_1+w_1-\mathcal{L}_2 w_1-\gamma w_1^3+\beta w_1\nabla_0^2 w_1. \tag{3.12}$$

In order for the function $w_3(\mathbf{x},t)$ to be nonsingular, the right-hand side of (3.12) cannot have a projection on the operator $\mathcal{L}_0^\dagger$ (the Fredholm alternative) [35]. This statement leads to the dynamics

$$\partial_T A_{11}=A_{11}+4(\mathbf{k}\cdot\tilde{\boldsymbol{\nabla}})^2 A_{11}-3\gamma|A_{11}|^2 A_{11} \tag{3.13}$$

of $A_{11}(\mathbf{X},T)$. The solution $w_3(\mathbf{x},t)$ of Eq. (3.12) is

$$w_3(\mathbf{x},t)=A_{30}+A_{31}e^{i\mathbf{k}\cdot\mathbf{x}}+A_{32}e^{2i\mathbf{k}\cdot\mathbf{x}}+A_{33}e^{3i\mathbf{k}\cdot\mathbf{x}}+\text{c.c.}, \tag{3.14}$$

where $A_{30}=-\beta|A_{11}|^2$, $A_{32}=-\frac{1}{9}\beta A_{11}^2$, and $A_{33}=-\frac{1}{64}\gamma {A_{11}}^3$. Application of the Fredholm alternative to expansions at order ϵ^4 and ϵ^5 gives

$$\begin{aligned}
\partial_T A_{21} &= A_{21}+4(\mathbf{k}\cdot\tilde{\boldsymbol{\nabla}})^2 A_{21}-4i(\mathbf{k}\cdot\tilde{\boldsymbol{\nabla}})\tilde{\nabla}^2 A_{11}\\
&\quad -3\gamma(A_{11}^2\bar{A}_{21}+2|A_{11}|^2 A_{21})
\end{aligned} \tag{3.15}$$

and

$$\begin{aligned}
\partial_T A_{31} &= A_{31}+4(\mathbf{k}\cdot\tilde{\boldsymbol{\nabla}})^2 A_{31}-4i(\mathbf{k}\cdot\tilde{\boldsymbol{\nabla}})\tilde{\nabla}^2 A_{21}\\
&\quad -3\gamma(A_{11}^2\bar{A}_{31}+2|A_{11}|^2 A_{31}+\bar{A}_{11}A_{33}\\
&\quad +2A_{11}|A_{21}|^2+\bar{A}_{11}A_{21}^2)\\
&\quad +\tilde{\nabla}^4 A_{11}-\tfrac{14}{9}\beta^2|A_{11}|^2 A_{11}).
\end{aligned} \tag{3.16}$$

respectively, for the dynamics of $A_{21}(\mathbf{X},T)$ and $A_{31}(\mathbf{X},T)$.

The envelope function $A_1(\mathbf{X},T)$ of the basic pattern $e^{i\mathbf{k}\cdot\mathbf{x}}$ is

$$A_1(\mathbf{X},T)=\epsilon A_{11}+\epsilon^2 A_{21}+\epsilon^3 A_{31}+\cdots. \tag{3.17}$$

We now deduce the amplitude equations for the dynamics of A_1 at the lowest order $O(\epsilon)$. Using Eq. (3.13) and scaling back to the original variables $\mathbf{x}\to\epsilon^{-1}\mathbf{X}$ and $t\to\epsilon^{-2}T$, we get

$$\partial_t A_1=\epsilon^2 A_1-3\gamma|A_1|^2 A_1+4(\mathbf{k}\cdot\tilde{\boldsymbol{\nabla}})^2 A_1. \tag{3.18}$$

Note that $A_1(\mathbf{x},t)$ is now considered to be function of the variables $\mathbf{x}$ and t. The amplitude equation for A_1 truncated at order $O(\epsilon^3)$, obtained by using Eqs. (3.13), (3.15), and (3.16) and scaling back to the original variables, is

$$\begin{aligned}
\partial_t A_1 &= \epsilon^2 A_1+4k_0^2\,\Box^2 A_1-(3\gamma-\tfrac{14}{9}\beta^2\epsilon^2)|A_1|^2 A_1\\
&\quad +\tfrac{3}{64}\gamma^2|A_1|^4 A_1,
\end{aligned} \tag{3.19}$$

where $\Box$ is the operator defined in (1.4).

The generalizations of the Swift-Hohenberg equations (3.1) and (3.2) are equivariant under the Euclidean symmetries. Let us follow the fate of the symmetries as we generate the amplitude equations through the multiple scale analysis. Equation (3.5) is invariant under all the symmetries, and thus if the perturbation expansion is carried out to all orders, the amplitude equations will be equivariant. However, this is generally not the case for finite truncations of the perturbation, e.g., Eq. (3.18) is not equivariant under arbitrary rotations. [The equivariance of Eq. (3.19), which depends on the particular form of the nonlinear term in (3.1), will be lost at the next order.] The origin of the nonequivariance of (3.18) lies in the term $(\mathbf{k}\cdot\tilde{\boldsymbol{\nabla}})^2 A_1$. But we notice from Eq. (3.19) that this term is a low-order approximation to $k_0^2\,\Box^2 A_1$. We propose in this section to regularize the expansion (3.18) by enforcing the rotational invariance. This can be done by replacing the nonequivariant term $(\mathbf{k}\cdot\tilde{\boldsymbol{\nabla}})^2 A_1$ by the equivariant term $k_0^2\,\Box^2 A_1$. The perturbation expansion truncated at any order can be regularized through this process, the equivariant form of each term being deduced by carrying out the perturbation to higher order. We refer to regularizing the perturbation expansion by imposing the correct symmetries on each term as symmetrizing. Equation (3.18), when symmetrized, gives

$$\partial_t A_1=\epsilon^2 A_1-3\gamma|A_1|^2 A_1+4k_0^2\,\Box^2 A_1. \tag{3.20}$$

We needed to add some (but not all) terms of order $O(\epsilon^2)$ and higher to Eq. (3.18) to generate amplitude equations

(3.20) that are equivariant under the required symmetries. Given that neither Eq. (3.20) nor Eq. (3.18) has the rigorous theoretical foundation of the normal form theory, we see no advantage of limiting the expansion up to a given order in perturbation at the risk of losing the equivariance of the amplitude equations. Perturbation expansions are valid only near the onset of patterns, while the physical system has the relevant symmetries for all parameters. Perhaps a more thorough analysis of the symmetry groups will lead to a perturbation scheme that will explicitly preserve the symmetries at each stage of the truncation.

In Appendix A we carry out the multiple scale expansion of the models (3.1) and (3.2) in the hexagonal basis (2.2). In particular we show how several nonlinear terms appearing in the low-order truncations are symmetrized by carrying out the expansions to higher order. The multiple scale expansion of Eq. (3.1) is shown to lead to amplitude equations that are equivalent to the Landau-Ginzburg equations (2.7) introduced in Sec. II. The expansion of Eq. (3.2) leads to different nonlinear coupling terms, and we show how they can be symmetrized.

The perturbation analysis described above is valid only when $\epsilon \ll 1$. As seen from Fig. 2, most of the interesting behavior, including stripe-hexagon competition, occurs far beyond this regime. In the absence of an alternative, we resort to using the Landau-Ginzburg equations as a model and study its properties for larger values of ϵ. Our numerical experiments support the assumption that the *qualitative behavior* of pattern formation remains unchanged when higher-order corrections are ignored, provided the amplitude equations are equivariant. However, with the low-order truncations we are unable to make any quantitative statements and we are restricted to making experimental comparisons with qualitative predictions of the theory.

IV. EXPERIMENTAL SYSTEM

Reaction-diffusion systems are particularly convenient for studies of pattern formation in planar nonequilibrium systems for the following reasons: (i) Large aspect ratios can easily be achieved; hence sidewall conditions do not strongly influence the patterns in the center of the reactor. In the present experiments the aspect ratio is typically 160 (the pattern wavelength is about 0.15 mm, while the reactor width is 25 mm). (ii) Arbitrary initial patterns can be generated by using light as a perturbation of a photosensitive reaction. We generate regular spatial patterns with different wavelengths and symmetries on a computer and then photograph these patterns and project them onto a planar reactor containing the photosensitive chlorite-iodide-malonic acid reaction. (iii) The pattern forming process is slow since the diffusion coefficients are small. Hence the development of a pattern can be followed in detail and the influence of the sidewalls can be neglected for long times (of the order of a day in our experiments). (iv) The pattern forms in a very thin band of the gel; thus the system is essentially two dimensional.

Our experiments use an open spatial reactor, as shown schematically in Fig. 3 [1,9,7,17]. The reaction occurs in a thin gel disk, 25.4 mm in diameter and 1.0 mm thick, made of polyvinyl alcohol or polyacrylamide. The gel prevents mass motion in the reaction medium; hence only reaction and diffusion processes are relevant for our study [9,10]. The gels have about 90% void space and an average pore size of about 10 nm. Thus small molecules such as chlorite, iodide, or malonic acid can diffuse nearly as freely in the gel as in water, while large molecules such as starch are essentially immobile. Different species in the gel can therefore have significantly different effective diffusion rates, which is necessary for a Turing instability [8,36]. To visualize patterns formed in the polyacrylamide gel, some soluble starch, an indicator for the CIMA reaction [6,9], was preloaded into the gel during preparation. Starch was not needed in the experiments using a polyvinyl alcohol gel since the gel itself is a CIMA reaction indicator [9].

The gel in the reactor is sandwiched between two thin membranes (Vycor porous glass disks from Corning or Anopore membranes from Whatman) [1,17,37]. The outer flat surface of each membrane is in contact with a continuously fed well-stirred tank reactor in which the concentration of chemicals and the temperature are maintained constant; see Fig. 3. The long time scales for pattern evolution (typically hours) facilitate the maintenance of uniform reservoir conditions.

The chlorite-iodide-malonic acid reaction exhibits a rich variety of nonlinear phenomena: bistability and oscillations in a batch reactor or in a stirred tank flow reactor [16], front structures in a Couette reactor [38], and Turing patterns in a spatial open reactor [16,39,7,17]. In the present experiments, components of the reaction are distributed in the two reservoirs in such a way that neither compartment is separately reactive. Chlorite resides

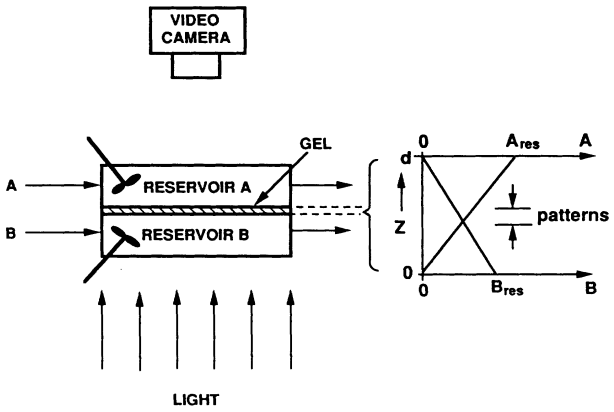

FIG. 3. Schematic diagram of the reactor for the reaction-diffusion experiments. The reaction occurs in the thin gel layer between reservoirs A and B. The concentrations A_{res} and B_{res} of the reagents in reservoirs A and B, respectively, are not separately reactive. Concentration gradients normal to the surface of the reactor are imposed so that the conditions needed to generate Turing patterns are satisfied in a layer that is much thinner than the gel thickness d; therefore the patterns observed in the experiments are quasi-two-dimensional.

only in reservoir A and malonic acid resides only in reservoir B. The other chemical species are contained in equal amounts in both reservoirs, except for sulfuric acid, which is more concentrated in reservoir B than in reservoir A.

The chemicals diffuse through the membranes into the gel where the reaction occurs. The chemical patterns form only in a thin planar region of the the 1 mm thick gel, as indicated in Fig. 3. The thickness of the pattern is comparable to the lattice spacing; hence the patterns are essentially two dimensional [40]. The patterns are monitored continuously in transmitted light. The data presented here are for the asymptotic states, reached after waiting 1–3 days following a change in control parameter. Digitized 480×512 pixel black and white images are processed and analyzed on a computer workstation.

V. RHOMBIC ARRAYS

In this section we demonstrate both theoretically and experimentally the existence of rhombic arrays in pattern forming systems. The rhombic arrays we consider can be obtained by stretching an array of regular hexagons along one of its six symmetry axes. Experimental realizations of hexagonal and rhombic arrays are shown in Fig. 4. As we argue below, the sixfold symmetry of regular hexagons is broken to the twofold symmetry of the rhombic array by the diffusion terms of the Landau-Ginzburg equations (2.7). The rhombic arrays form via spontaneous symmetry breaking in systems that are invariant under the Euclidean symmetries and consequently they can point in any direction. The characteristic angles of stable rhombic arrays occur in a band about the 60° of regular hexagons, e.g., in Fig. 4(d) the angle is 66°. A

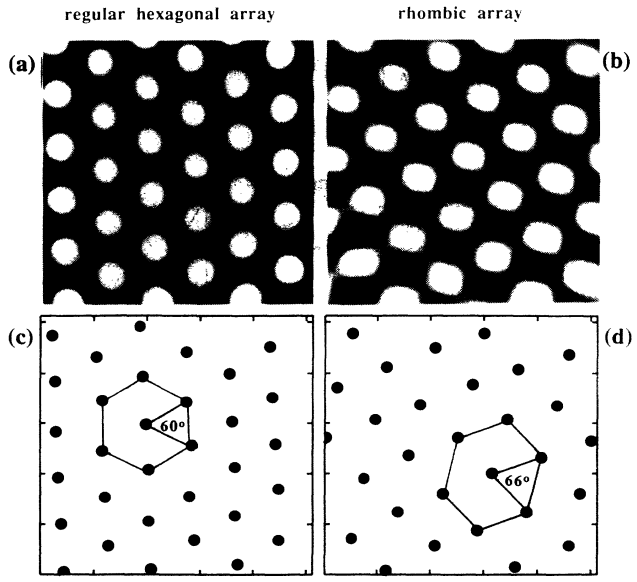

FIG. 4. Examples of (a) hexagonal and (b) rhombic patterns observed in the experiments. Diagrams (c) and (d) show the local maxima and characteristic angles of the hexagonal and rhombic arrays, respectively.

physical system evolving from a noisy initial state will in general contain multiple domains of rhombic arrays, each with its own orientation and characteristic angle. Multistability distinguishes our rhombic arrays from the "nonequilateral hexagonal patterns" introduced recently [41].

The general theory is presented in the following subsection and the predictions are compared with an experiment in Sec. V B.

A. The theory of rhombic arrays

A rhombic array obtained by stretching a hexagonal array along one of its six symmetry axes has its point group symmetry reduced from D_6 to D_2. In the analysis below, we stretch a hexagonal array along the x direction, which is chosen to be one of the symmetry axes. The transformation is achieved by the operator

$$\mathcal{S} : (x, y) \rightarrow ((1+\bar{\delta})^{-1}x, y). \tag{5.1}$$

The field $U_R(\mathbf{x}, t)$ characterizing the resulting rhombic array can be expanded as

$$U_R(\mathbf{x}, t) = \sum_{n=1}^{3} a_n e^{i\mathbf{k}_n \cdot (\mathcal{S}^{-1}\mathbf{x})}. \tag{5.2}$$

Noting that $\mathbf{k}_1 \cdot (\mathcal{S}^{-1}\mathbf{x}) = \mathbf{k}_1 \cdot \mathbf{x}$, $\mathbf{k}_2 \cdot (\mathcal{S}^{-1}\mathbf{x}) = \mathbf{k}_2 \cdot \mathbf{x} + \frac{\sqrt{3}}{2}\bar{\delta}x$, and $\mathbf{k}_3 \cdot (\mathcal{S}^{-1}\mathbf{x}) = \mathbf{k}_3 \cdot \mathbf{x} - \frac{\sqrt{3}}{2}\bar{\delta}x$, we deduce that the envelope functions for the rhombic array, expanded in the hexagonal basis (2.2), are

$$A_1 = a_1, \quad A_2 = a_2 e^{i\delta x}, \quad A_3 = a_3 e^{-i\delta x}, \tag{5.3}$$

where $\delta = \frac{\sqrt{3}}{2}\bar{\delta}$. The envelope function formalism is valid only if the envelope functions A_n are slowly varying, i.e, for sufficiently small δ. However, we expect the qualitative results to hold for a larger range of parameters.

For simplicity we study the existence and stability of the solutions of type (5.2) of the Landau-Ginzburg equations for the variational case, $\nu = 0$ in (2.7). The conclusions presented below continue to be valid for nonzero ν. The envelope functions (5.3) with $a_1 = \text{const}$ and $a_2 = a_3 = \text{const}$ are solutions of (2.7) when a_1 and a_2 are solutions of

$$\mu a_1 + \alpha a_2^2 - a_1(a_1^2 + 2\rho a_2^2) = 0,$$
$$\mu - \gamma\left(\frac{\sqrt{3}}{2}\delta + \frac{\delta^2}{2k_0}\right)^2 + \alpha a_1 - (1+\rho)a_2^2 - \rho a_1^2 = 0. \tag{5.4}$$

The hexagonal solution can be retained by setting $a_1 = a_2$. Below we determine the domain of linear stability of the solution (5.4).

Let us digress briefly to discuss the relevance of the linear stability of the rhombic state. The analysis below will show that out of all the linearly stable rhombic arrays, hexagons have the largest growth rate (starting from the uniform state). Furthermore, in the variational case ($\nu = 0$), the hexagons will have minimum "energy"

[as given by (2.8)] among all the rhombic arrays. Then why are rhombic arrays seen in experiment? We believe that the initial conditions of the system play a significant role in determining the equilibrium state of the system. Thus, if a system with variational dynamics starts in a rhombic state, it will have to create or destroy cells (via phase slips) in order to move towards a hexagonal state of *lower energy*. In order to do this, the system has to move over a large *local* energy barrier. Typically, physical systems do not change their structure if they are linearly stable. (An array of rolls in Rayleigh-Bénard convection can reach stationary states for a band of wave vectors [42].). What we suggest, and what is supported by the experimental observations, is that as long as the rhombic array is linearly stable it will not change its structure. The relevance of linear stability of the rhombic state follows.

The domain of linear stability of the rhombic solution (5.3) is determined by spectral decomposition. The rhombic pattern is perturbed to $\tilde{A}_1 = a_1 + (u_1 + iv_1)$, $\tilde{A}_2 = [a_2 + (u_2 + iv_2)]e^{i\delta x}$, and $\tilde{A}_3 = [a_2 + (u_3 + iv_3)]e^{-i\delta x}$ and the perturbations (u_n, v_n) are expanded as $(u_n, v_n) = (u_n^{(0)}, v_n^{(0)})e^{\omega t + i\mathbf{K}\cdot\mathbf{x}}$. With these substitutions (2.7) reduces to a matrix equation

$$\omega\ \mathbf{w}^T = \mathbf{M}\cdot\mathbf{w}^T, \tag{5.5}$$

where $\mathbf{w} = (u_1^{(0)}, v_1^{(0)}, u_2^{(0)}, v_2^{(0)}, u_3^{(0)}, v_3^{(0)})$ and $\mathbf{M} = (m_{ij})$ is a 6×6 matrix. We need to find the range of parameters (μ, δ) for which the solution is stable (i.e., $\omega < 0$) against all long wavelength perturbations. Except for $\mathbf{K} = \mathbf{0}$ the domain of linear stability has to be calculated numerically. In the domain shown in Fig. 5, the eigenvalues of the matrix $\mathbf{M}$ are negative for values of $|\mathbf{K}| < 0.25k_0$. For each set of parameters we have checked the eigenvalues for 10 values of $|\mathbf{K}| < 0.25k_0$ and for 20 directions $\hat{\mathbf{K}}$.

The calculation of the eigenvalues for $\mathbf{K} = \mathbf{0}$ provide some insight about the boundaries of the stability domain. For $\mathbf{K} = \mathbf{0}$, the nonzero matrix coefficients of $\mathbf{M}$ are

$$\begin{aligned}
m_{11} &= \mu - 3a_1^2 - 2\rho a_2^2,\\
m_{13} &= \alpha a_2 - 2\rho a_1 a_2,\\
m_{22} &= \mu - a_1^2 - 2\rho a_2^2,\\
m_{24} &= -\alpha a_2,\\
m_{33} &= \mu - \gamma\left(\frac{\sqrt{3}}{2}\delta + \frac{\delta^2}{2k_0}\right)^2 - 3a_2^2 - \gamma(a_1^2 + a_2^2),\\
m_{35} &= \alpha a_1 - 2\gamma a_2^2,\\
m_{44} &= m_{33} + 2a_2^2,\\
m_{46} &= -\alpha a_1.
\end{aligned} \tag{5.6}$$

Two eigenvalues of $\mathbf{M}$ are

$$\omega_1 = m_{44} - m_{46}, \quad \omega_2 = m_{33} - m_{35}, \tag{5.7}$$

while a pair (ω_3, ω_4) is given by

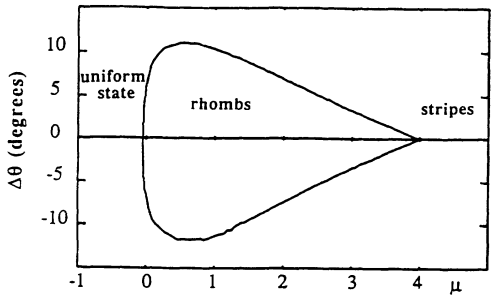

FIG. 5. The domain of linearly stable rhombic arrays of Eq. (2.7) with $\alpha = 1$, $\rho = 2$, and $\nu = 0$. The vertical axis denotes the deviation $\Delta\theta$ of the characteristic angle of the rhombic array from the 60° angle of regular hexagons. This stability domain appears in a "third" dimension in the stability domain for hexagons in Fig. 2.

$$\Delta_1 = \det\begin{pmatrix} m_{11} - \omega & 2m_{13} \\ m_{13} & m_{33} + m_{35} - \omega \end{pmatrix} = 0. \tag{5.8}$$

The final pair of eigenvalues (ω_5, ω_6) satisfies

$$\Delta_2 = \det\begin{pmatrix} m_{22} - \omega & 2m_{24} \\ m_{24} & m_{44} + m_{46} - \omega \end{pmatrix} = 0. \tag{5.9}$$

ω_1 and one solution of $\Delta_2 = 0$ (say, ω_5) vanish, confirming the marginality of the rhombic array under two translations. ω_6 is always negative. The left boundary of the stability domain of Fig. 5 is determined by the existence of the rhombic solution (5.4) while the right boundary corresponds to ω_3 becoming positive; ω_2 and ω_4 are negative inside the stability domain.

The quantitative form of the boundary of the stability domain depends on the coefficients of Eq. (2.7) and on the terms retained. However, some qualitative features appear to be universal. For example, at each end of the stability domain the band of stable rhombs collapses to regular hexagons and the stability band widens as one moves away from each end of the stability domain. These qualitative stability properties should hold for rhombic arrays in a wide range of pattern forming systems. One might inquire if the stability of rhombic arrays will be lost on introducing higher-order terms in the perturbation expansion. It can be shown that this is not the case. The existence of a stable hexagonal array implies that all eigenvalues of the hexagonal state are negative, except for the two that correspond to the translational modes. For a sufficiently small perturbation of the array (stretching along a symmetry axis) the negative eigenvalues remain so, while the marginal eigenvalues continue to be zero. Thus the only possible motion of the rhombic array is translation. It can be shown using the theory of relative equilibria [43,44] that there is no translation of a rhombic array. Thus rhombic arrays formed by a sufficiently small stretching of the hexagonal array will be linearly stable. The result depends only on the group structure and the continuity of the perturbation.

Why have rhombic arrays not been reported in the many studies of pattern forming systems (e.g., Bénard-

Marangoni convection or Rayleigh-Bénard convection in non-Boussinesq fluids)? The probable reason is that only regular hexagons would form in experiments where the control parameter is slowly varied. Beginning in the uniform state, a slow variation of the control parameter [e.g., μ in the model (2.7)] leads to the transition where only the hexagons are stable at the onset of instability. The hexagons remain linearly stable as the control parameter is further increased quasistatically and thus rhombic arrays will not be seen through such a process. One way to get a rhombic array is to change the control parameter discontinuously into the interior of the stability domain of hexagons. This is how rhombic arrays were originally discovered in the experiments on the CIMA reaction [1].

B. Predictions and comparison with experiment

Figure 6 shows large arrays of hexagons and rhombs generated by imposing as a perturbation an optical pattern with a particular symmetry. The wavelength of the perturbation was chosen to be the natural wavelength, as determined from Fourier transforms of patterns formed from random initial conditions. The patterns in Fig. 6 are *stable*—they persist indefinitely after the optical perturbation is removed. An arbitrary direction can be chosen for the orientation of these arrays, reflecting the invariance of our system under rotations. The form of the envelope functions (i.e., $|A_2| = |A_3| \neq |A_1|$) of the rhombic state implies that four of the six peaks in the spatial Fourier transform for the rhombic state will have equal magnitude while the other two will have a different magnitude; in contrast, for an array of regular hexagons all spectral components will have the same magnitude. Figures 6(c) and 6(d) confirm these expectations. This type of Fourier spectrum for rhombic arrays has also been observed in numerical simulations [45]. The relative heights of the amplitudes is model dependent. In our model, it can be determined from the solution of Eq. (5.4) for a given characteristic angle.

The predicted form of the stability domain (Fig. 5) was

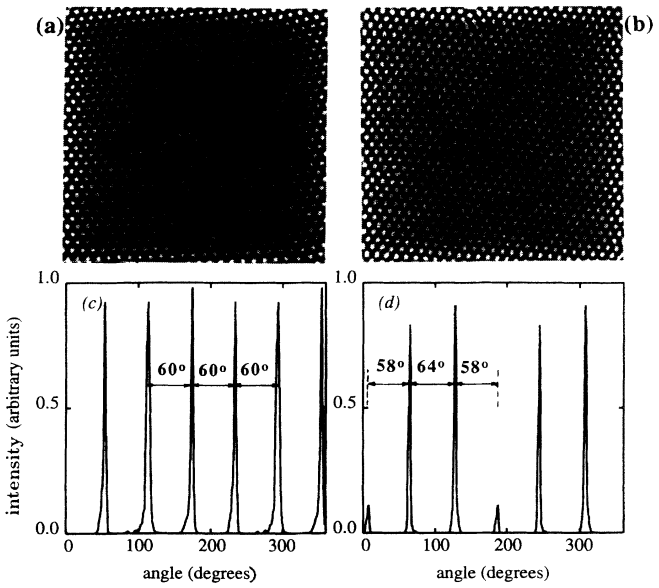

FIG. 6. (a) Hexagonal and (b) rhombic arrays obtained in the experiments; (c) and (d) show the corresponding angular intensity distributions in spatial frequency space in bands centered at an intrinsic wave vector of 5.5 mm^{-1}. The patterns were initially generated by illuminating the photosensitive reaction medium with light in the desired test pattern. After this perturbation was removed, these patterns remained stable asymptotically. The chemical concentrations in reservoirs A and B on the two sides of the reactor are $[CH_2(COOH)_2]_0^B = 32$ mM, $[I^-]_0^{A,B} = 2.2$ mM, $[Na_2SO_4]_0^{A,B} = 4.5$ mM, $[ClO_2^-]_0^A = 22$ mM, $[H_2SO_4]_0^A = 1$ mM, $[H_2SO_4]_0^B = 20$ mM, and temperature 7.0 °C. The region shown is 6 mm × 6 mm.

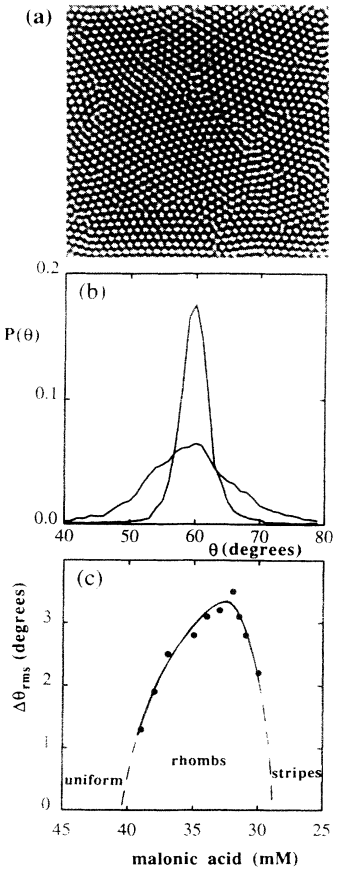

FIG. 7. (a) Extended stationary chemical pattern with domains of rhombic arrays with different characteristic angles in a band near 60°. The control parameters were the same as in Fig. 6, except $[CH_2(COOH)_2]_0^B = 32$ mM; the region shown is 6 mm × 6 mm. (b) Distribution of angles observed in patterns at two values of the malonic acid concentration. The narrow distribution, which has a root-mean-square width of 2.3°, was observed not far beyond the onset of patterns, $[CH_2(COOH)_2]_0^B = 39$ mM; the broad distribution, which has a rms width of 4.5°, was obtained further away from the transition, $[CH_2(COOH)_2]_0^B = 32$ mM. (c) The root-mean-square width of the distribution of angles $\Delta\theta_{rms}$ observed in the chemical patterns as a function of the bifurcation parameter, the malonic acid concentration in reservoir B.

tested in the experiments with optical perturbations. For a given value of control parameter, the gel reactor was illuminated with intense light in a perfect rhombic lattice of dots, with characteristic angles ranging from 45° to 75°. (Again, the wavelength of the perturbation was carefully chosen to be the intrinsic wavelength.) Perturbations with regular hexagonal patterns (characteristic angles of 60°) were always found to be stable beyond the bifurcation to patterns. However, rhombic patterns were stable only if the characteristic angle was not significantly different from 60°. Figure 7(a) shows a pattern that formed asymptotically after the removal of an unstable rhombic pattern, one with a characteristic angle outside of the stable band: the system rearranged itself into multiple domains, each of which contained a rhombic array with a characteristic angle inside the stable band [37]. The distribution of characteristic angles in such a pattern depends on the control parameter. As shown in Figs. 7(b) and 7(c), the root-mean-square width $\Delta\theta_{rms}$ of the distribution increases as one moves away from the onset of patterns. Figure 7(c) is in good qualitative accord with the theoretical prediction in Fig. 5. A quantitative comparison of experiment and theory would require the evaluation of the coefficients in the Landau-Ginzburg equation from the chemical kinetics and diffusion coefficients of the reaction and perhaps the inclusion of higher-order terms in the perturbation expansion.

VI. BLACK-EYE PATTERNS

For experimental conditions different from those used in the experiments described in the preceding section, a complex black-eye pattern emerges well beyond the primary instability; examples of these patterns are shown in Figs. 8(a)–8(c). We have investigated mainly black-eye patterns with regular hexagonal symmetry, but at the end of this section we will mention observations of similar patterns that form from rhombic patterns.

The black-eye patterns result from a resonant interaction between the basic modes of the hexagonal array. These patterns consist of two hexagonal lattices: one of white spots and the other of black spots at the center of each white spot and at the center of the dark region in each equilateral triangle with three neighboring white spots at its vertices. The hexagonal lattice of white spots has a wavelength of 0.15 mm while the lattice of black dots has a wavelength 0.086 mm. The ratio of the two wavelengths is $\sqrt{3}$, suggesting that the lattice of black spots is a harmonic structure of the lattice of white spots. The spatial Fourier transform in Fig. 9 supports this interpretation.

A phase diagram showing the transition from hexagons to black-eye patterns and then to stripes is shown in Fig. 10. The control parameter for these experiments is the malonic acid concentration in reservoir B; all other parameters are fixed at the values given in the caption for Fig. 8. The primary instability of the uniform state occurs when the malonic acid concentration is increased above $[CH_2(COOH)_2]_0^B = 7.0$ mM. At a higher concentration, $[CH_2(COOH)_2]_0^B \approx 8.0$ mM, the spatial harmonics corresponding to the black-eye patterns become detectable in the Fourier spectra and faint black dots become visible in the center of each white dot [see Fig. 8(a)]. The amplitude of the harmonics increases as the control parameter is increased and becomes quite large, as the photograph in Fig. 8(b) and the graph in Fig. 10(b) illustrate. The amplitude of the harmonics reaches a maximum at $[CH_2(COOH)_2]_0^B \approx 10.5$ mM and then decreases gradually to zero, at which point the system undergoes a transition to stripes [see Fig. 8(d)]. The transition from hexagons to the black-eye patterns is nonhysteretic within the mesh in control parameter, 0.5 mM, while the transition from black-eye patterns to stripes is hysteretic, as illustrated by the hysteresis loop in Fig. 10(a).

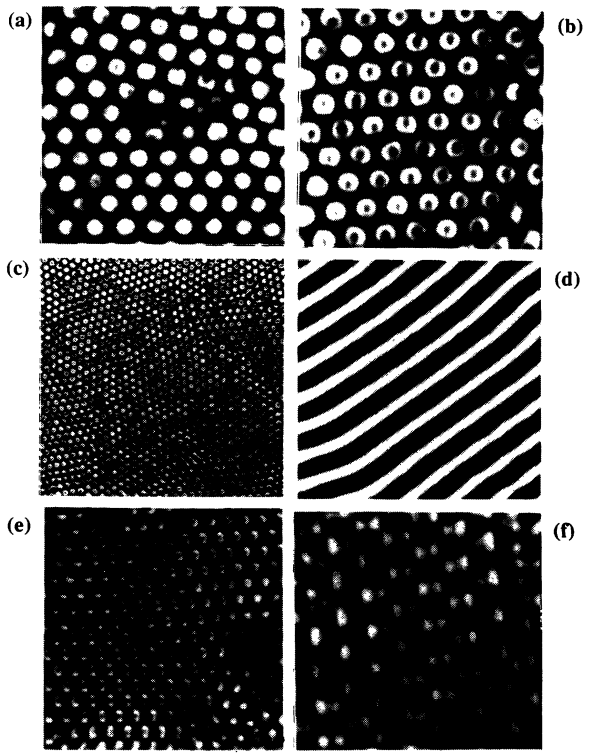

FIG. 8. "Black-eye" patterns: (a) Just beyond the transition point; $[CH_2(COOH)_2]_0^B = 8$ mM. (b) Fully developed black eyes; $[CH_2(COOH)_2]_0^B = 12$ mM. (c) Large array of black eyes for the same conditions as in (b). (d) Striped pattern that appears when the black-eye pattern becomes unstable; $[CH_2(COOH)_2]_0^B = 15$ mM. (e) and (f) two-fold symmetric black-eye patterns observed with $[CH_2(COOH)_2]_0^B = 12.5$ mM and $[CH_2(COOH)_2]_0^B = 13.5$ mM, respectively. The patterns were observed in a 10% polyvinyl alcohol gel disk sandwiched between two Vycor porous glass disks. The other parameters were fixed at the following values: $[I^-]_0^{A,B} = 3$ mM, $[Na_2SO_4]_0^{A,B} = 4.5$ mM, $[ClO_2^-]_0^A = 22$ mM, $[H_2SO_4]_0^A = 2$ mM for (a)–(d), $[H_2SO_4]_0^A = 1$ mM for (e) and (f), $[H_2SO_4]_0^B = 20$ mM, and temperature 7.0 °C. The regions shown in (a), (b), (d), and (f) are 1.6 mm × 1.6 mm, while those shown in (c) and (e) are 6 mm × 6 mm. The fundamental and anharmonic wavelengths of the black eyes shown in (b) are 0.086 mm and 0.15 mm, respectively.

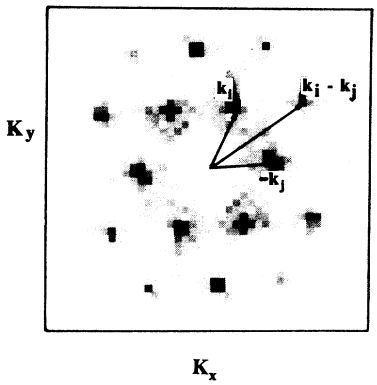

FIG. 9. Two-dimensional spatial Fourier transform of Fig. 8(b), showing the harmonic wave vectors that are responsible for the black-eye patterns.

The observation of the harmonic structures indicates a need to go beyond the "fundamental representation" in the description of the black-eye patterns [19,24]. Appendix A presents a multiple scale analysis of the Swift-Hohenberg equation that shows how resonances between the basic modes of the hexagonal patterns can lead to the generation of the secondary modes. Close to the onset, the secondary modes are negligible and the pattern can be described using the fundamental representation (2.1). As shown in Appendix A, the most significant secondary modes are those observed in our experiments: wave vectors $(\mathbf{k}_i - \mathbf{k}_j)$ and $2\mathbf{k}_i$ (see Fig. 9). However, the analysis suggests that the amplitude of the harmonics should grow continuously beyond the primary instability, while in the experiments the harmonics were not detected until well beyond onset of hexagons, as shown in the diagram in Fig. 10(b). We do not understand this difference between theory and experiment. We may simply not have sufficient sensitivity to detect the harmonics closer to the onset of the primary instability, or perhaps the secondary modes are not "slaved" to the primary modes.

For other experimental conditions we have observed harmonic structures arising from rhombic rather than hexagonal patterns. Figures 8(e) and 8(f) are examples of these two-fold symmetric patterns with harmonic structure. We have not examined in detail the transitions leading to and from these patterns.

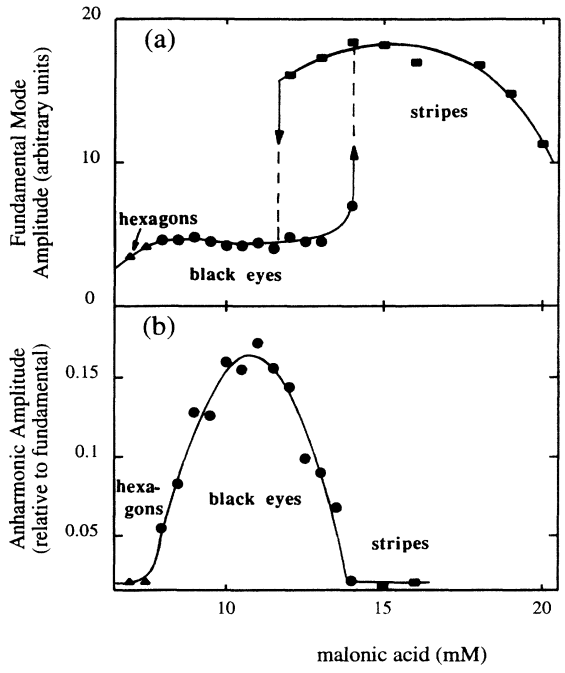

FIG. 10. (a) Transition diagram showing regimes with hexagons, black eyes, and stripes as a function of the malonic acid concentration in reservoir B (all other conditions were fixed at the values given in Fig. 8). (b) Amplitude of the spatial harmonics relative to the fundamental. Symbols: ▲, hexagons; •, black eyes; ■, stripes.

VII. DYNAMICS OF DOMAIN WALLS AND COMPLEX STATES

As indicated in the Introduction, the rotational invariance of the amplitude equations is essential to the study of multiple domains of stripes pointing in arbitrary directions. Approximations that do not preserve the symmetry exactly could lead to qualitatively incorrect patterns through the choice of preferred directions. In this section we demonstrate in numerical simulations that the behavior of domain walls for models equivariant under rotations is *qualitatively* different from that for nonequivariant models. We also present dynamics of a complex pattern consisting of multiple domains of stripes and hexagons. Similar behavior has been observed in patterns generated in the reaction-diffusion system.

The time evolution of the Landau-Ginzburg equation (2.7) is studied numerically using the alternating direction implicit algorithm [46]. Each nonlinear term $N[A(\mathbf{x},t)]$ is expanded to linear order in $\delta A = A(\mathbf{x}, t+\delta t) - A(\mathbf{x},t)$, thus linearizing the equations in $A(\mathbf{x}, t+\delta t)$. The cross derivatives, such as $\partial^4 A_1/\partial x^2 \partial y^2$, are calculated explicitly. The results presented here are from the evolution of A_k's on a 32×32 lattice with periodic boundary conditions. The slow variables A_k are interpolated to a 128×128 lattice on which $U(\mathbf{x},t)$ is evaluated using (2.1). The domain is chosen to have a length of 4π in each direction and k_0 is 4.0. Each time step was 0.01 units and it was checked in several cases that smaller time steps do not change the conclusions.

The equivariant dynamics is generated by (2.7), while the nonequivariant dynamics is modeled by the substitution

$$\Box_n \rightarrow \hat{\mathbf{k}}_n \cdot \nabla \tag{7.1}$$

in the Landau-Ginzburg equations. This and several other nonequivariant models have been studied numerically before [32,47,48]. The domain wall generated by nonequivariant dynamics [Fig. 11(b)] is very abrupt, while that generated by equivariant dynamics [Fig. 11(a)] is smooth, like the domain walls in the experiments. Although the parameters chosen for the integration are well beyond the range of applicability of the

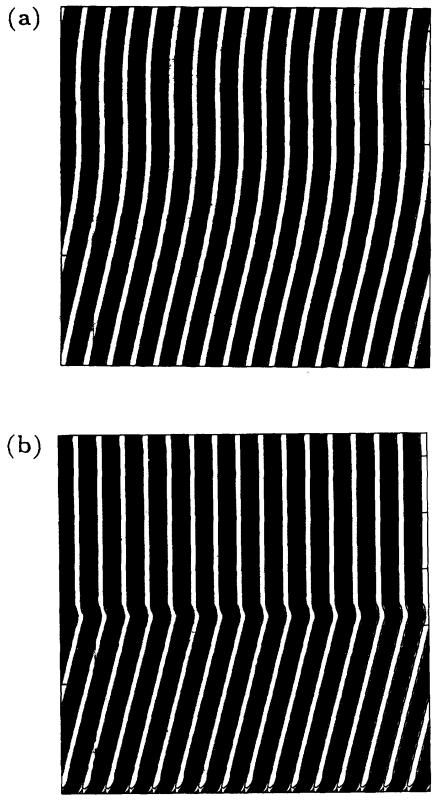

FIG. 11. The shape of domain walls is qualitatively different for (a) equivariant and (b) nonequivariant models. In the initial state, stripes in the upper half plane point in the y direction, while those in the lower half plane are slanted to the y direction. The equivariant dynamics is generated by the Landau-Ginzburg equations with $\alpha = 1$, $\rho = 2$, $\mu = 6$, $\gamma = 0.1$, and $\nu = 0$, while the nonequivariant dynamics is obtained by replacing $\Box_n$ by $(\hat{\mathbf{k}}_n \cdot \nabla)$. The pattern of (a) is reminiscent of the experimental patterns [cf., e.g., Figs. 1 and 8(d)], while the boundary in (b) is abrupt.

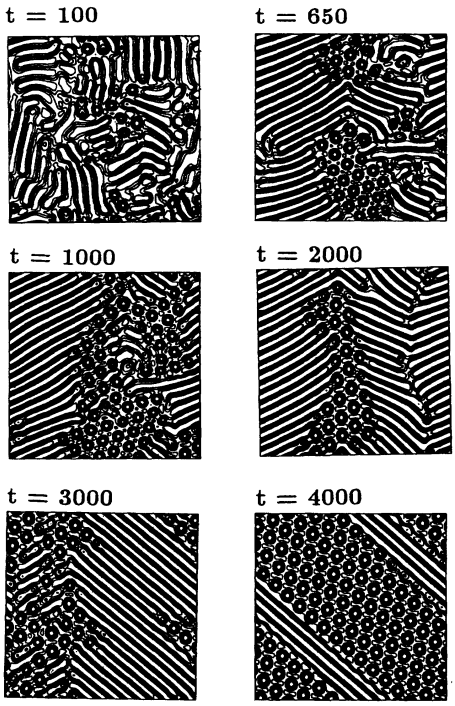

FIG. 12. A sequence of patterns generated by the numerical integration of the equivariant amplitude equations (2.7) with periodic boundary conditions, random initial conditions, and parameters $\alpha = 1$, $\rho = 2$, $\mu = 6$, $\gamma = 0.1$, and $\nu = -0.195$. Hexagonal and striped domains invade each other over a long time before the hexagons dominate the pattern. In what appears to be the final (stationary) state ($t = 4000$), a single line of stripes separates two hexagonal domains of different orientations.

perturbation expansion, it appears, at least for this case, that the symmetrized amplitude equations give qualitatively correct patterns. It would be extremely interesting to determine if this is valid generally.

Figure 12 shows patterns generated by numerical integration of the Landau-Ginzburg equations (2.7) for a set of parameters where both hexagons and stripes are linearly stable. (For the parameters given in the caption of Fig. 12, the bistable domain is $1 < \mu < 4$.) The equivariance of the model implies that stripes (as well as hexagons) pointing in *any* direction are equivalent; thus the physical system is not in a simple bistable state. Domains of hexagons and stripes invade each other over a long time (compared to the diffusion time) before the pattern settles down. For the example shown, the (apparent) asymptotic state consists of two hexagonal domains separated by a set of stripes. The hexagons in the two domains have different orientations, but by the rotational symmetry have the same stability. The domain wall between the states consists of stripes, which is the "metastable state." Qualitatively similar dynamics is seen for a small range of the parameters. We have observed this complex behavior only in the presence of nonvariational terms [i.e., $\nu \neq 0$ in (2.7)].

Similar behavior of the dynamics of a domain wall is observed in the experiments on the CIMA reaction, as Fig. 13 illustrates. Each domain invades the other as in the numerical integration Fig. 12. Again this behavior is observed only for a narrow range of control parameters in the bistable region. It is not known if the patterns in Fig. 13 continue to evolve or reach a stationary state; continuous evolution would mean that the system is nonvariational.

We end this section with a discussion of patterns generated from the numerical integration of (2.7) from a random initial state when stripes are the only stable periodic array (i.e., $\mu > 4$ for parameters of Fig. 12). The patterns generated by both nonvariational and variational equations, illustrated in Figs. 14(a) and 14(b), respectively, fail to reach an extended uniform state, in contrast to the situation when both hexagons and stripes are stable. Local patches develop into independent arrays of stripes pointing in arbitrary directions. The domain sizes in the patterns increase with the "diffusion coefficient" γ. When different domains run into each other,

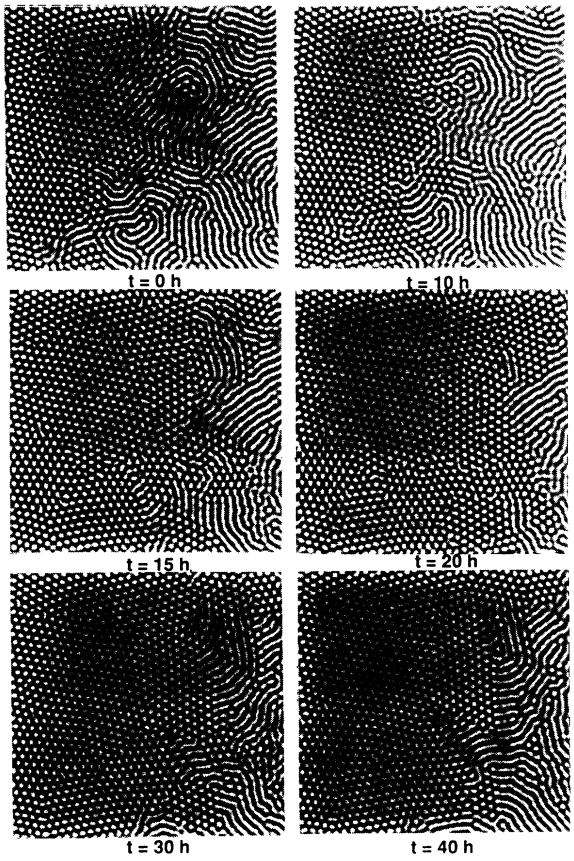

FIG. 13. This sequence of patterns observed in the experiment shows oscillatory movement of the boundary between hexagonal and striped domains. This type of behavior was observed in a narrow parameter range near the hexagon-stripe transition point. The chemical concentrations in reservoirs A and B were $[CH_2(COOH)_2]_0^B = 32$ mM, $[I^-]_0^{A,B} = 3.0$ mM, $[Na_2SO_4]_0^{A,B} = 4.5$ mM, $[ClO_2^-]_0^A = 22$ mM, $[H_2SO_4]_0^A = 1$ mM, $[H_2SO_4]_0^B = 20$ mM, and temperature 7.0 °C. The region shown is 6 mm × 6 mm.

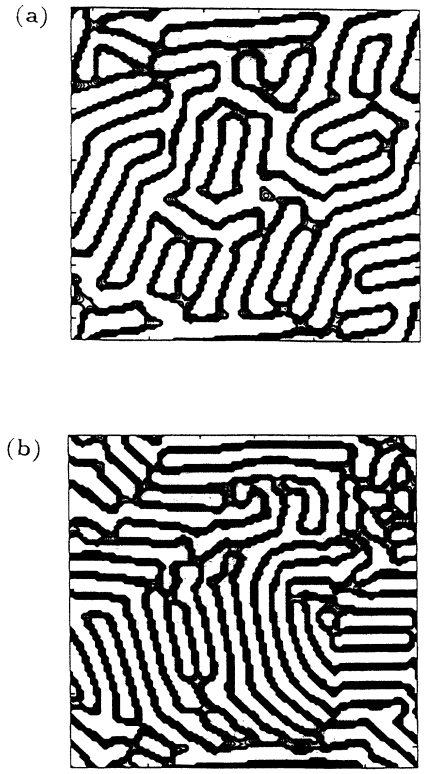

FIG. 14. Patterns generated from the numerical integration of (a) nonvariational and (b) variational Landau-Ginzburg equations (2.7) with random initial conditions. The nonvariational patterns are time dependent and do not appear to settle down, while the variational patterns appear to be stationary with neighboring domains making an angle close to 120° with each other. The domain is of length 4π in each direction and periodic boundary conditions are imposed. Parameter values: (a) $k_0 = 4.0$, $\alpha = 1.0$, $\rho = 2$, $\gamma = 0.1$, $\mu = 6$, and $\nu = -0.19$; (b) the same as in (a) except for $\mu = 8$, $\gamma = 2$, and $\nu = 0$.

the isotropy allows for the rolls to bend at the boundary and join smoothly rather than forming sharp domain walls.

Numerical integration of (2.7) for the nonvariational case (i.e., $\nu \neq 0$) yields patterns in which the stripes change direction smoothly and *rounded domains* are observed; see Fig. 14(a). These patterns apparently never settle down, i.e., they are time dependent. Close to the onset of stripes (e.g., $\mu \sim 5$) the pattern evolves relatively fast, while further away from the onset (e.g., $\mu \sim 10$) the evolution is very slow. These properties are reminiscent of patterns observed in the CIMA reaction (Fig. 1) and in Rayleigh-Bénard convection.

For the variational case [i.e., $\nu = 0$ in (2.7)], the patterns appear to reach a stationary state, even though $U(\mathbf{x}, t)$ exhibits small ($\sim 0.1\%$) fluctuations due to the finiteness of the time step δt of integration. (These fluctuations decrease with decreasing δt.) Individual domains are defined much better than in the nonvariational case, and the domain walls appear to be sharper. In most cases, the stripes in neighboring domains form an angle close to 120° with each other. Similar qualitative properties are observed in patterns on magnetic bubbles and ferrofluids, both of which are governed by variational dynamics.

VIII. DISCUSSION

We have presented a theoretical and experimental study of extended patterns generated through a Turing bifurcation. The theory was developed in the amplitude equation formalism and was restricted to systems that are invariant under translations, rotations, and reflections. The primary results, deduced on the basis of the symmetries, are the equivariant amplitude equations (1.5) and (2.7). These equations should serve as general models for studies of universal features of patterns in di-

verse systems in the presence of Euclidean symmetries.

In Sec. III, we introduced a modification of the multiple scale expansion of Newell-Whitehead-Segel that was constructed to give equivariant amplitude equations. The expansions were carried out for two variations of the Swift-Hohenberg equations. We also showed that our theory is equivalent to the Cross-Newell theory, and we deduced an equivariant generalization of the Pomeau-Manneville phase equation.

On the basis of the theory, we deduced the existence of linearly stable rhombic arrays. These can point in arbitrary directions and occur in a band of characteristic angles about the 60° angle of regular hexagons. We demonstrated their existence in a reaction-diffusion system with a chlorite-iodide-malonic acid reaction. The experiments supported several predictions of the theory. We predict that rhombic arrays will be observed in other pattern forming systems as well.

We needed to move beyond the fundamental representation (2.1) in order to characterize the black-eye patterns observed in the reaction-diffusion system. Bifurcations to and from the black-eye states were described with Fourier spectra and secondary modes were shown to appear as "slaved" variables in the multiple scale expansion of the Swift-Hohenberg equation. Discrepancies between the theory and the experiments suggest that the assumption of "slaving" of the secondary modes to the primary modes may need to be relaxed.

The equivariance of the amplitude equations is essential in the study of complex patterns such as Fig. 1. Our deduction of the amplitude equations was forced by the requirement of the equivariance under arbitrary rotations. An alternative approach has used models of the characterizing field [49], such as the Swift-Hohenberg equation; however, this approach cannot describe individual bifurcations such as the Turing bifurcation. In Sec. VII, we presented the results of numerical integration of the amplitude equations (2.7). We demonstrated the necessity of the equivariance by studying the behavior of domain walls, and we observed differences between variational and nonvariational dynamics.

In conclusion, we hope that our theoretical and experimental study will stimulate further work on the consequences of Euclidean symmetries on pattern formation in planar systems.

ACKNOWLEDGMENTS

We have benefited from discussions with Jacques Boissonade, Pierre Borckmans, Stephen Davis, Patrick De Kepper, Martin Golubitsky, Kyoung Lee, W.D. McCormick, Boris Malomed, Michael Marder, Ian Melbourne, and Alan Newell. G.H.G. acknowledges partial support from the Office of Naval Research (through Grant No. N-00014-K-0613) and from the Institute of Space Sciences Operations at the University of Houston. Q.O. and H.L.S. acknowledge the support of the Department of Energy Office of Basic Energy Sciences and the Robert A. Welch Foundation.

APPENDIX A: DERIVATION OF AMPLITUDE EQUATIONS IN A HEXAGONAL BASIS

We outline how the multiple scale expansion is regularized for the generalizations

$$\partial_t U(\mathbf{x},t) = \left[\epsilon^2 - (1+\nabla^2)^2\right]U(\mathbf{x},t) - \gamma[U(\mathbf{x},t)]^3 + \epsilon\beta U(\mathbf{x},t)\nabla^2 U(\mathbf{x},t) \quad \text{(A1)}$$

and

$$\partial_t U(\mathbf{x},t) = \left[\epsilon^2 - (1+\nabla^2)^2\right]U(\mathbf{x},t) - \gamma[U(\mathbf{x},t)]^3 + \epsilon\beta[\boldsymbol{\nabla} U(\mathbf{x},t)]^2 \quad \text{(A2)}$$

of the Swift-Hohenberg equation in the hexagonal basis (2.2). We will show how the terms appearing at the lowest order in perturbation can be symmetrized to give amplitude equations that are equivariant under the Euclidean symmetries. The multiple scale expansion of (A1) leads to a set of amplitude equations which are equivalent to Eq. (2.7) introduced in Sec. II, while the expansion of (A2) gives different nonlinear coupling terms. The scaling

$$X = \epsilon x \ , \ Y = \epsilon y \ , \ T = \epsilon^2 t \quad \text{(A3)}$$

introduced in Sec. III simplifies the perturbation analysis considerably. As in Sec. III, we write the scalar field $U(\mathbf{x},t)$ as

$$U(\mathbf{x},t) = \epsilon w_1(\mathbf{x},t) + \epsilon^2 w_2(\mathbf{x},t) + \epsilon^3 w_3(\mathbf{x},t) + \cdots \quad \text{(A4)}$$

and expand the envelope functions $A_n(\mathbf{x},t)$

$$A_n(\mathbf{x},t) = \epsilon A_{11}^{(n)} + \epsilon^2 A_{21}^{(n)} + \epsilon^3 A_{31}^{(n)} + \cdots, \quad \text{(A5)}$$

where $A_{ml}^{(n)}$ is the coefficient of $e^{li\mathbf{k}_n\cdot\mathbf{x}}$ in the Fourier expansion of $w_m(\mathbf{x},t)$.

At order ϵ^1, the expansion of (3.1) gives $\mathcal{L}_0 w_1 = 0$, implying

$$w_1(\mathbf{x},t) = \sum_{n=1}^{3} A_{11}^{(n)} e^{i\mathbf{k}_n\cdot\mathbf{x}} + \text{c.c.}, \quad \text{(A6)}$$

with $|\mathbf{k_n}| = 1$. At order ϵ^2, the expansion gives $\mathcal{L}_0 w_2 + \mathcal{L}_1 w_1 = 0$, which results in

$$w_2(\mathbf{x},t) = \sum_{n=1}^{3} A_{21}^{(n)} e^{i\mathbf{k}_n\cdot\mathbf{x}} + \text{c.c.} \quad \text{(A7)}$$

As in Sec. III, all expansions are carried out in a single hexagonal basis $\{\mathbf{k}_n\}$ in order to study modulations on a hexagonal pattern. At order ϵ^3 we get

$$\mathcal{L}_0 w_3 = -\partial_T w_1 + w_1 - \mathcal{L}_2 w_1 - \gamma w_1^3 + \beta w_1 \nabla_0^2 w_1. \quad \text{(A8)}$$

The Fredholm alternative implies that coefficient of $e^{i\mathbf{k}_n\cdot\mathbf{x}}$ vanishes for each n. For $n = 1$ we get

$$\partial_T A_{11}^{(1)} = A_{11}^{(1)} + 4(\mathbf{k}_1\cdot\tilde{\boldsymbol{\nabla}})^2 A_{11}^{(1)} + 2\beta\bar{A}_{11}^{(2)}\bar{A}_{11}^{(3)} - 3\gamma(|A_{11}^{(1)}|^2 + 2|A_{11}^{(2)}|^2 + 2|A_{11}^{(3)}|^2)A_{11}^{(1)}. \quad \text{(A9)}$$

The equations for the dynamics of $A_{11}^{(2)}$ and $A_{11}^{(3)}$ can be deduced by cyclic permutations. The solution $w_3(\mathbf{x},t)$ can be written as

$$w_3(\mathbf{x},t) = A_{30}^{(n)} + \sum_1 (A_{31}^{(n)} e^{i\mathbf{k}_n\cdot\mathbf{x}}) + \sum_2 (B_{nm} e^{i(2\mathbf{k}_n+\mathbf{k}_m)\cdot\mathbf{x}} + C_{nm} e^{i(2\mathbf{k}_n-\mathbf{k}_m)\cdot\mathbf{x}}) + \sum_1 (A_{32}^{(n)} e^{2i\mathbf{k}_n\cdot\mathbf{x}}) + \sum_1 (A_{33}^{(n)} e^{3i\mathbf{k}_n\cdot\mathbf{x}}), \quad \text{(A10)}$$

where $\sum_1$ is the summation over $n = 1,2,3$ and $\sum_2$ is the summation over $n,m = 1,2,3$ with $m \neq n$. The coefficients $A_{30}^{(n)}$, $A_{31}^{(n)}$, $A_{32}^{(n)}$, B_{nm}, and C_{nm} can be written explicitly in terms of the coefficients defined earlier. A straightforward but long calculation at the next order in perturbation gives the symmetrized amplitude equation [after rescaling through $\mathbf{x} \to \epsilon\mathbf{X}$ and $t \to \epsilon^2 T$ and using the definition (A5)]

$$\partial_t A_1(\mathbf{x},t) = \epsilon^2 A_1 + 4\,\Box_1^2 A_1 + 2\epsilon\beta \bar{A}_2 \bar{A}_3 - 3\gamma(|A_1|^2 + 2|A_2|^2 + 2|A_3|^2)A_1 + 2i\epsilon\beta(\bar{A}_2 \bar{\Box}_3 \bar{A}_3 + \bar{A}_3 \bar{\Box}_2 \bar{A}_2) \quad \text{(A11)}$$

and the corresponding equations for A_2 and A_3. The last term can be converted to $\bar{\Box}_2 \bar{A}_2 \bar{\Box}_3 \bar{A}_3$ by a trivial rescaling of the basic length scale k_0. Notice that the nonlinear coupling term $i[\bar{A}_2(\mathbf{k}_3\cdot\boldsymbol{\nabla})\bar{A}_3 + \bar{A}_3(\mathbf{k}_2\cdot\boldsymbol{\nabla})\bar{A}_2]$ that appears at lower order in perturbation [32] (and renders the amplitude equation non-equivariant) is symmetrized to $i(\bar{A}_2\bar{\Box}_3\bar{A}_3 + \bar{A}_3\bar{\Box}_2\bar{A}_2)$.

The multiple scale expansion of (A2) gives the amplitude equation

$$\partial_t A_1(\mathbf{x},t) = \epsilon^2 A_1 + 4\,\Box_1^2 A_1 + 2\epsilon\beta \bar{A}_2 \bar{A}_3 - 3\gamma(|A_1|^2 + 2|A_2|^2 + 2|A_3|^2)A_1 + 2\epsilon\beta\Big\{ i(\bar{A}_2(\mathbf{k}_2\cdot\boldsymbol{\nabla})\bar{A}_3 + \bar{A}_3(\mathbf{k}_3\cdot\boldsymbol{\nabla})\bar{A}_2) - (\boldsymbol{\nabla}\bar{A}_2)(\boldsymbol{\nabla}\bar{A}_3)\Big\}, \quad \text{(A12)}$$

with corresponding equations for A_2 and A_3. Once again these amplitude equations are equivariant under arbitrary rotations. We also note that the nonlinear coupling term $i[\bar{A}_2(\mathbf{k}_2\cdot\boldsymbol{\nabla})\bar{A}_3 + \bar{A}_3(\mathbf{k}_3\cdot\boldsymbol{\nabla})\bar{A}_2]$ appearing at the lowest order in the perturbation expansion can be symmetrized to give equivariant dynamics. The equivariance of the nonlinear coupling term in (A12) can be traced back to the restriction of the expansions to hexagonal bases. In contrast, the equivariance of terms, such as $\Box^2 A(\mathbf{x},t)$, are a consequence of the invariance of $(\sin^2\theta + \cos^2\theta)$.

Finally, we notice from Eq. (A10) that $w_3(\mathbf{x},t)$ and hence $U(\mathbf{x},t)$ contain Fourier components other than A_n. We thus have to go beyond the "fundamental representation" in order to describe such patterns. (See case study 4 of Ref. [19].) The spectral components closest in magnitude to the *excited modes* correspond to the wave vectors of type $2\mathbf{k}_n$ and $(\mathbf{k}_n - \mathbf{k}_m)$. As we move beyond the onset, we expect to see the effects of these spectral components. They give additional structure to the basic building blocks of the hexagonal array [24]. We believe that the black-eye patterns described in Sec. VI are the first reported experimental observations of these states.

APPENDIX B: COMPARISON WITH CROSS-NEWELL EQUATIONS

The Cross-Newell theory [25,34] describes patterns that are locally roll-like almost everywhere. The pattern $U(\mathbf{x},t)$ is assumed to be of the form $U(\mathbf{x},t) = Ae^{i\theta}$, where $\mathbf{k} = \nabla\theta$ is normal to the local orientation of rolls. The perturbation parameter is the ratio η^2 of the roll size to the size of the container, with $0 < \eta^2 \ll 1$. The *slow variables* are defined by

$$\mathbf{X} = \eta^2\mathbf{x}\ ,\ T = \eta^4 t\ ,\ \Theta(\mathbf{X},T) = \eta^2\theta(\mathbf{x},t). \quad \text{(B1)}$$

As shown in Ref. [25], for the Swift-Hohenberg equation, the perturbation expansion up to order $O(\eta^6)$ gives

$$\Theta_T A^2 + \boldsymbol{\nabla}\cdot(\mathbf{k}B) + \eta^4 A(D_1\cdot D_2 + D_2\cdot D_1)A = 0, \quad \text{(B2)}$$

where $B = A^2\frac{dA^2}{dk^2}$. The operators D_1 and D_2 are defined by $D_1 = 2\mathbf{k}\cdot\boldsymbol{\nabla} + (\boldsymbol{\nabla}\cdot\mathbf{k})$ and $D_2 = \nabla^2$. Like the model (2.7), the Cross-Newell theory is equivariant under rotations and is complementary to it in the following sense. It is valid for a larger range of parameters (from the onset of patterns), but is limited to the study of slowly varying stripes. In contrast, the model (2.7) can be used to study more general structures, e.g., an array of slowly varying hexagons or a complex pattern consisting of stripes and hexagons. In this appendix we will outline a proof that the Cross-Newell theory is equivalent to (1.5) in the common domain of validity. We make no pretense at completeness and freely use the results and notation of Ref. [25]. In fact, a knowledge of Sec. 2 of Ref. [25] is essential to follow the rest of the appendix.

As argued in Ref. [25], the "amplitude" A of a slowly varying array of stripes can be considered to be constant. In contrast to Ref. [25] and in the spirit of the work described here, we let the normal to the stripes point at an angle ψ_0 to the local coordinates (ξ,ζ). A neighboring point has a wave vector $\mathbf{k}$ (perturbed from $\mathbf{k}_0$) pointing at an angle ψ with the local basis. Then the variable Θ is given by [see Eq. (2.46) of Ref. [25]]

$$\Theta = k_0[\xi\cos(\psi_0) + \zeta\sin(\psi_0)] + \eta^2\phi(\xi,\zeta,T), \quad \text{(B3)}$$

from which we deduce that

$$\Theta_\xi = k_0\cos(\psi_0) + \eta^2\phi_\xi, \qquad \Theta_\zeta = k_0\sin(\psi_0) + \eta^2\phi_\zeta. \quad \text{(B4)}$$

The variation in the wave vector is now given by

$$(k^2 - k_0^2) = 2\eta^2 k_0(\hat{\mathbf{k}}_0\cdot\boldsymbol{\nabla}\phi) + \eta^4\nabla^2\phi, \quad \text{(B5)}$$

where $\hat{\mathbf{k}}_0 = \hat{\xi}\cos(\psi_0) + \hat{\zeta}\sin(\psi_0)$ and ∇ is expanded in the local basis. More algebra leads to

$$\begin{aligned}\nabla\cdot[\mathbf{k}(k^2-k_0^2)] = {} & 2k_0^2\eta^2(\hat{\mathbf{k}}_0\cdot\nabla)^2\phi \\ & +k_0\eta^4\left[2(\nabla^2\phi)(\hat{\mathbf{k}}_0\cdot\nabla)\phi\right. \\ & \left.+(\hat{\mathbf{k}}_0\cdot\nabla)(\nabla\phi)^2+(\hat{\mathbf{k}}_0\cdot\nabla)\phi\nabla^2\phi\right] \\ & +\eta^6\left[(\nabla^2\phi)(\nabla\phi)^2+(\nabla\phi)\cdot\nabla^3\phi\right]. \quad \text{(B6)}\end{aligned}$$

Finally scaling variables back according to $t \to \eta^{-4}T$ and $\mathbf{x} \to \eta^{-2}\mathbf{X}$ gives

$$\begin{aligned}\phi_t = {} & 4k_0^2(\hat{\mathbf{k}}_0\cdot\nabla)^2\phi + 2k_0((\hat{\mathbf{k}}_0\cdot\nabla)\phi)(\nabla^2\phi) \\ & +2k_0(\hat{\mathbf{k}}_0\cdot\nabla)(\nabla\phi)^2 + 2k_0(\nabla^2\phi)((\hat{\mathbf{k}}_0\cdot\nabla)\phi) \\ & -4k_0(\nabla\phi)((\hat{\mathbf{k}}_0\cdot\nabla)\nabla\phi) - 2(\nabla^2\phi)(\nabla\phi)^2 \\ & -(\nabla^4\phi). \quad \text{(B7)}\end{aligned}$$

This is easily seen to be the imaginary part of

$$\partial_t W = 4\,\Box^2 W + \epsilon W - |W|^2 W \quad \text{(B8)}$$

with $W(\mathbf{x},t) = A(\mathbf{x},t)e^{i\phi(\mathbf{x},t)}$. This is what we set out to prove. Note that (B7) is the rotationally invariant generalization of the phase equation of Pomeau and Manneville [26].

[1] Q. Ouyang and H. L. Swinney, Chaos **1**, 411 (1991).
[2] M. S. Heutmaker and J. P. Gollub, Phys. Rev. A **35**, 242 (1987).
[3] R. E. Rosensweig, J. Magn. Magn. Mater. **39**, 127 (1983).
[4] D. Sornette, J. Phys. (Paris) **48**, 151 (1987); C. Kooy and U. Enz, Philips Res. Rep. **15**, 7 (1960); P. Molho, J. Gouzerh, J. C. S. Levy, and J. L. Porteseil, J. Magn. Magn. Mater. **54**, 857 (1987); K. L. Babcock and R. M. Westervelt, Phys. Rev. A **40**, 2022 (1989).
[5] A. Turing, Philos. Trans. R. Soc. London Ser. B **237**, 37 (1952).
[6] V. Castets, E. Dulos, and P. De Kepper, Phys. Rev. Lett. **64**, 2953 (1990); P. De Kepper, V. Castets, E. Dulos, and J. Boissonade, Physica D **49**, 161 (1991).
[7] Q. Ouyang and H. L. Swinney, Nature **352**, 610 (1991).
[8] I. Lengyel, S. Kádár, and I. R. Epstein, Phys. Rev. Lett. **69**, 2729 (1992).
[9] Z. Noszticzius, Q. Ouyang, W. D. McCormick, and H. L. Swinney, J. Phys. Chem. **96**, 6303 (1992).
[10] Z. Noszticzius, W. Horsthemke, W. D. McCormick, H. L. Swinney, and W. Y. Tam, Nature **329**, 619 (1987).
[11] A. C. Newell and J. A. Whitehead, J. Fluid Mech. **38**, 279 (1969); L. A. Segel, *ibid.* **38**, 203 (1969).
[12] A. C. Newell, in *Lectures in the Sciences of Complexity*, edited by D. L. Stein (Addison-Wesley, Menlo Park, CA, 1989), p. 107.
[13] P. Coullet, C. Elphick, and D. Repaux, Phys. Rev. Lett. **58**, 431 (1987).
[14] K. J. Lee, W. D. McCormick, Q. Ouyang, and H. L. Swinney, Science **261**, 192 (1993).
[15] E. Moses and V. Steinberg, Phys. Rev. Lett. **57**, 2018 (1986); P. Le Gal, A. Pocheau, and V. Croquette, *ibid.* **54**, 2501 (1985).
[16] P. De Kepper, J. Boissonade, and I. R. Epstein, J. Phys. Chem. **94**, 6525 (1990).
[17] Q. Ouyang and H. L. Swinney, in *Chemical Waves and Patterns*, edited by R. Kapral and K. Showalter (Kluwer, Dordrecht, 1994).
[18] J. Guckenheimer and P. Holmes, *Nonlinear Oscillations, Dynamical Systems, and Bifurcations of Vector Fields* (Springer-Verlag, New York, 1983).
[19] M. Golubitsky, I. Stewart, and D. G. Schaeffer, *Singularities and Groups in Bifurcation Theory* (Springer-Verlag, New York, 1988), Vol. 2.
[20] F. H. Busse and R. M. Clever, J. Fluid Mech. **91**, 319 (1979).
[21] J. B. Swift and P. C. Hohenberg, Phys. Rev. A **15**, 319 (1977).
[22] R. Camassa and D. D. Holm, Phys. Rev. Lett. **76**, 1661 (1993).
[23] See G. T. Mason, *Many Particle Physics*, 2nd ed. (Plenum, New York, 1990), Chap. 5.
[24] B. Dionne and M. Golubitsky, Z. Angew. Math. Phys. **43**, 36 (1992); K. Kirchgässner, Math. Methods Appl. Sci. **1**, 453 (1979).
[25] M. C. Cross and A. C. Newell, Physica D **10**, 299 (1984).
[26] Y. Pomeau and P. Manneville, J. Phys. Lett. **40**, L609 (1979).
[27] E. Buzano and M. Golubitsky, Philos. Trans. R. Soc. London Ser. A **308**, 617 (1983).
[28] S. Ciliberto, P. Coullet, J. Lega, E. Pampaloni, and C. Perez-Garcia, Phys. Rev. Lett. **65**, 2370 (1990).
[29] H. R. Brand, P. S. Lomdahl, and A. C. Newell, Physica D **23**, 345 (1986).
[30] G. H. Gunaratne, Phys. Rev. Lett. **71**, 1367 (1993).
[31] $U(\mathcal{R}^{-1}\mathbf{x}) = \sum A_n(\mathcal{R}^{-1}\mathbf{x})e^{i\mathbf{k}_n\cdot(\mathcal{R}^{-1}\mathbf{x})} = \sum A_n(\mathcal{R}^{-1}\mathbf{x}) \times e^{i(\mathcal{R}\mathbf{k}_n)\cdot\mathbf{x}} = \sum[A_n(\mathcal{R}^{-1}\mathbf{x})[e^{i\Delta\mathbf{k}_n\cdot\mathbf{x}}]e^{i\mathbf{k}_n\cdot\mathbf{x}}$.
[32] H. R. Brand, Prog. Theor. Phys. Suppl. **99**, 442 (1989).
[33] G. Sivashinsky, Annu. Rev. Fluid Mech. **15**, 179 (1983).
[34] A. C. Newell, T. Passot, and J. Lega, Annu. Rev. Fluid Mech. **25**, 399 (1993).
[35] P. Manneville, *Dissipative Structures and Weak Turbulence* (Academic, New York, 1990).
[36] J. E. Pearson and W. J. Bruno, Chaos **2**, 513 (1992).
[37] Q. Ouyang, G. H. Gunaratne, and H. L. Swinney, Chaos **3**, 707 (1993).
[38] Q. Ouyang, V. Castets, J. Boissonade, J. C. Roux, P. De Kepper, and H. L. Swinney, J. Phys. Chem. **95**, 351 (1991).
[39] V. Castets, E. Dulos, J. Boissonade, and P. De Kepper, Phys. Rev. Lett. **64**, 2953 (1990).
[40] Q. Ouyang, Z. Noszticzius, and H. L. Swinney, J. Phys. Chem. **96**, 6773 (1992).
[41] B. A. Malomed, A. A. Nepomnyashchy, and A. E. Nuz, Physica D **70**, 357 (1994).
[42] F. H. Busse, J. Math. Phys. **46**, 140 (1967); J. Fluid Mech. **30**, 625 (1967)
[43] M. Field, Trans. Am. Math. Soc. **259**, 185 (1980).
[44] M. Kruppa, SIAM J. Math. Anal. **21**, 1253 (1990).
[45] V. Dufiet and J. Boissonade, J. Chem. Phys. **96**, 664 (1992); V. Dufiet and J. Boissonade, Physica A **188**, 158

(1992).
[46] W. H. Press, B. P. Flannery, S. A. Teukolsky, and W. T. Vettering, *Numerical Recipes—The Art of Scientific Computing* (Cambridge University Press, Cambridge, England, 1988).
[47] Y. Tu and M. C. Cross, Phys. Rev. Lett. **69**, 2515 (1992).
[48] B. A. Malomed, A. A. Nepomnyashchy, and M. I. Tribelsky, Phys. Rev. A **42**, 7244 (1990).
[49] H. S. Greenside, W. M. Coughran, and N. L. Schryer, Phys. Rev. Lett. **49**, 726 (1982).

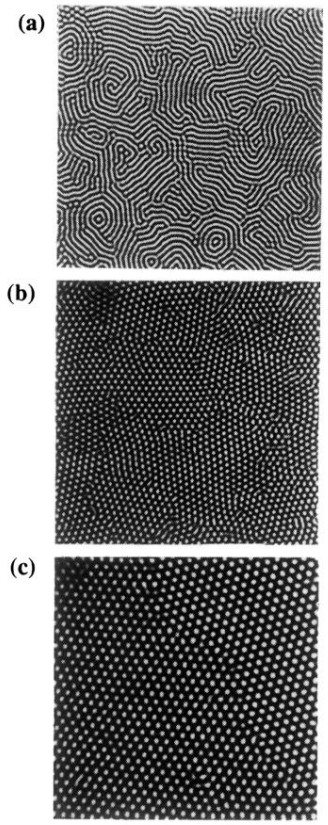

FIG. 1. Chemical patterns observed in a quasi-two-dimensional reaction-diffusion system with the chlorite-iodide-malonic acid reaction: (a) multiple domains of stripes, (b) multiple domains of hexagons of different orientations, and (c) a pattern with a single grain boundary separating hexagonal lattices with different orientations. The reaction occurs in a thin polyvinyl alcohol layer contained between two reservoirs. The wavelength of the patterns are (a) 0.11 mm, (b) 0.12 mm, and (c) 0.18 mm. The region shown is a 6 mm $\times$ 6 mm section of the 25 mm diam reactor. The malonic acid concentrations in reservoir B were (see Fig. 3) (a) 27 mM, (b) 24 mM, and (c) 32 mM. Other control parameters were held fixed at $[I^-]_0^{A,B} = 2.2$ mM, $[Na_2SO_4]_0^{A,B} = 4.5$ mM, $[ClO_2^-]_0^A = 22$ mM, $[H_2SO_4]_0^A = 1$ mM, $[H_2SO_4]_0^B = 20$ mM, and temperature 7.0 °C.

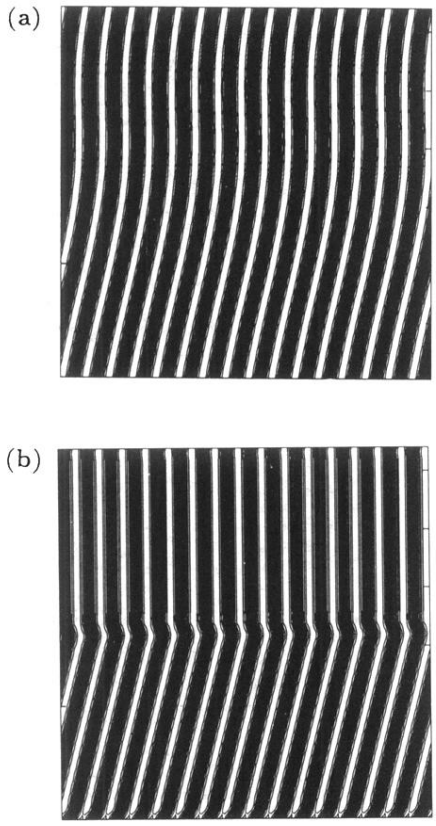

FIG. 11. The shape of domain walls is qualitatively different for (a) equivariant and (b) nonequivariant models. In the initial state, stripes in the upper half plane point in the y direction, while those in the lower half plane are slanted to the y direction. The equivariant dynamics is generated by the Landau-Ginzburg equations with $\alpha = 1$, $\rho = 2$, $\mu = 6$, $\gamma = 0.1$, and $\nu = 0$, while the nonequivariant dynamics is obtained by replacing $\Box_n$ by $(\hat{\mathbf{k}}_n \cdot \boldsymbol{\nabla})$. The pattern of (a) is reminiscent of the experimental patterns [cf., e.g., Figs. 1 and 8(d)], while the boundary in (b) is abrupt.

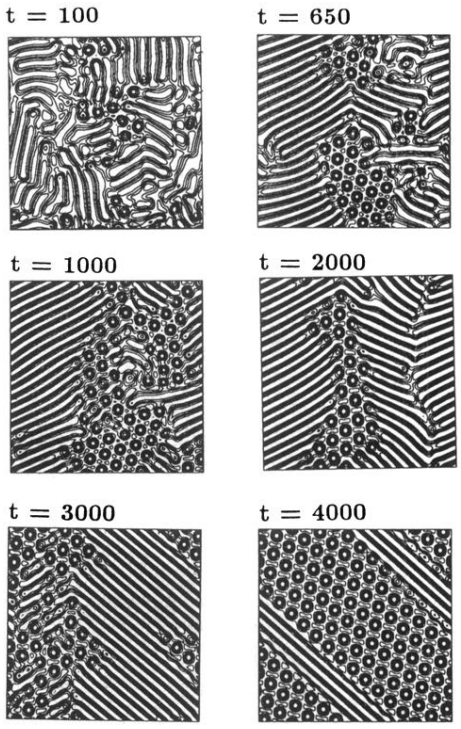

FIG. 12. A sequence of patterns generated by the numerical integration of the equivariant amplitude equations (2.7) with periodic boundary conditions, random initial conditions, and parameters $\alpha = 1$, $\rho = 2$, $\mu = 6$, $\gamma = 0.1$, and $\nu = -0.195$. Hexagonal and striped domains invade each other over a long time before the hexagons dominate the pattern. In what appears to be the final (stationary) state ($t = 4000$), a single line of stripes separates two hexagonal domains of different orientations.

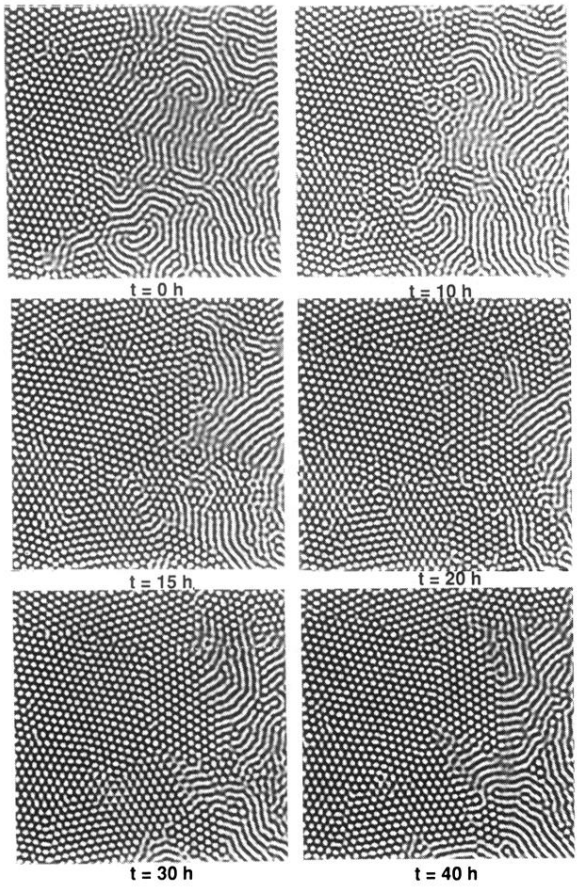

FIG. 13. This sequence of patterns observed in the experiment shows oscillatory movement of the boundary between hexagonal and striped domains. This type of behavior was observed in a narrow parameter range near the hexagon-stripe transition point. The chemical concentrations in reservoirs A and B were $[CH_2(COOH)_2]_0^B = 32$ mM, $[I^-]_0^{A,B} = 3.0$ mM, $[Na_2SO_4]_0^{A,B} = 4.5$ mM, $[ClO_2^-]_0^A = 22$ mM, $[H_2SO_4]_0^A = 1$ mM, $[H_2SO_4]_0^B = 20$ mM, and temperature 7.0 °C. The region shown is 6 mm × 6 mm.

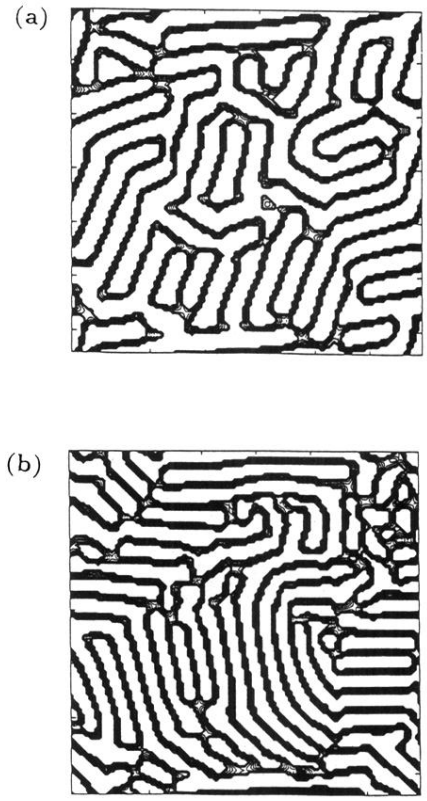

FIG. 14. Patterns generated from the numerical integration of (a) nonvariational and (b) variational Landau-Ginzburg equations (2.7) with random initial conditions. The nonvariational patterns are time dependent and do not appear to settle down, while the variational patterns appear to be stationary with neighboring domains making an angle close to 120° with each other. The domain is of length 4π in each direction and periodic boundary conditions are imposed. Parameter values: (a) $k_0 = 4.0$, $\alpha = 1.0$, $\rho = 2$, $\gamma = 0.1$, $\mu = 6$, and $\nu = -0.19$; (b) the same as in (a) except for $\mu = 8$, $\gamma = 2$, and $\nu = 0$.

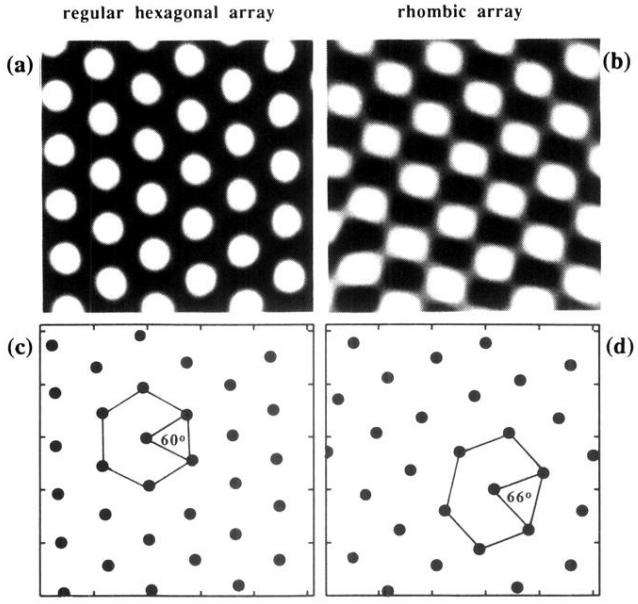

FIG. 4. Examples of (a) hexagonal and (b) rhombic patterns observed in the experiments. Diagrams (c) and (d) show the local maxima and characteristic angles of the hexagonal and rhombic arrays, respectively.

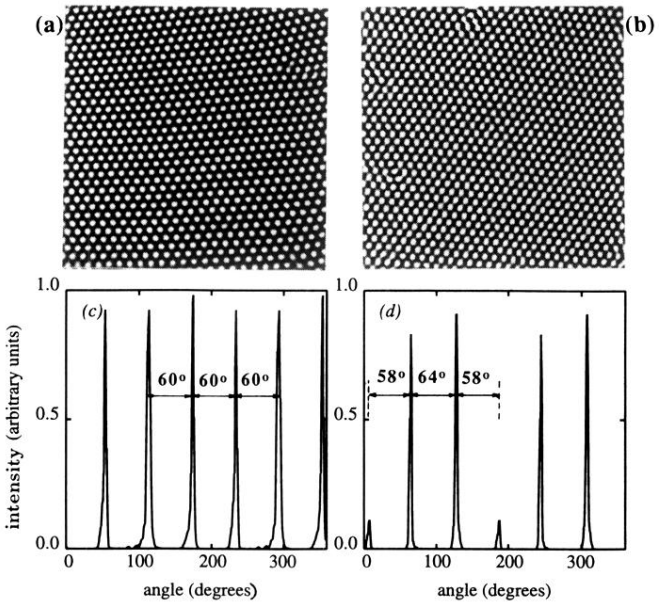

FIG. 6. (a) Hexagonal and (b) rhombic arrays obtained in the experiments; (c) and (d) show the corresponding angular intensity distributions in spatial frequency space in bands centered at an intrinsic wave vector of 5.5 mm^{-1}. The patterns were initially generated by illuminating the photosensitive reaction medium with light in the desired test pattern. After this perturbation was removed, these patterns remained stable asymptotically. The chemical concentrations in reservoirs A and B on the two sides of the reactor are $[CH_2(COOH)_2]_0^B = 32$ mM, $[I^-]_0^{A,B} = 2.2$ mM, $[Na_2SO_4]_0^{A,B} = 4.5$ mM, $[ClO_2^-]_0^A = 22$ mM, $[H_2SO_4]_0^A = 1$ mM, $[H_2SO_4]_0^B = 20$ mM, and temperature 7.0 °C. The region shown is 6 mm × 6 mm.

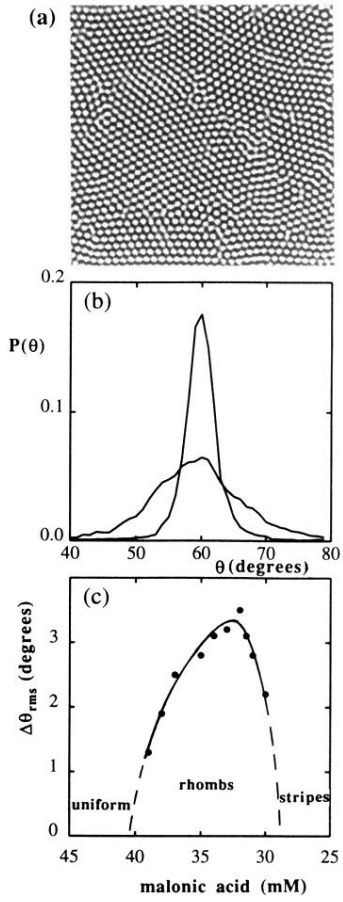

FIG. 7. (a) Extended stationary chemical pattern with domains of rhombic arrays with different characteristic angles in a band near 60°. The control parameters were the same as in Fig. 6, except $[CH_2(COOH)_2]_0^B = 32$ mM; the region shown is 6 mm × 6 mm. (b) Distribution of angles observed in patterns at two values of the malonic acid concentration. The narrow distribution, which has a root-mean-square width of 2.3°, was observed not far beyond the onset of patterns, $[CH_2(COOH)_2]_0^B = 39$ mM; the broad distribution, which has a rms width of 4.5°, was obtained further away from the transition, $[CH_2(COOH)_2]_0^B = 32$ mM. (c) The root-mean-square width of the distribution of angles $\Delta\theta_{rms}$ observed in the chemical patterns as a function of the bifurcation parameter, the malonic acid concentration in reservoir B.

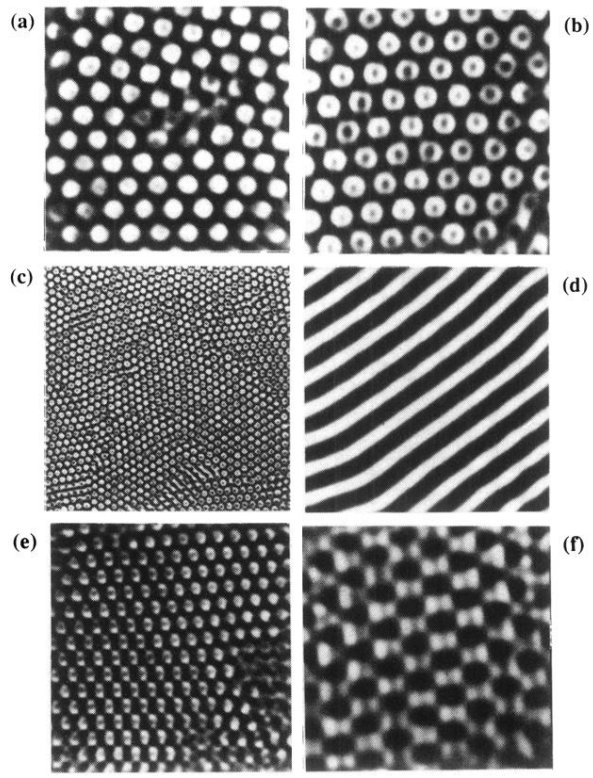

FIG. 8. "Black-eye" patterns: (a) Just beyond the transition point; $[CH_2(COOH)_2]_0^B = 8$ mM. (b) Fully developed black eyes; $[CH_2(COOH)_2]_0^B = 12$ mM. (c) Large array of black eyes for the same conditions as in (b). (d) Striped pattern that appears when the black-eye pattern becomes unstable; $[CH_2(COOH)_2]_0^B = 15$ mM. (e) and (f) two-fold symmetric black-eye patterns observed with $[CH_2(COOH)_2]_0^B = 12.5$ mM and $[CH_2(COOH)_2]_0^B = 13.5$ mM, respectively. The patterns were observed in a 10% polyvinyl alcohol gel disk sandwiched between two Vycor porous glass disks. The other parameters were fixed at the following values: $[I^-]_0^{A,B} = 3$ mM, $[Na_2SO_4]_0^{A,B} = 4.5$ mM, $[ClO_2^-]_0^A = 22$ mM, $[H_2SO_4]_0^A = 2$ mM for (a)–(d), $[H_2SO_4]_0^A = 1$ mM for (e) and (f), $[H_2SO_4]_0^B = 20$ mM, and temperature 7.0 °C. The regions shown in (a), (b), (d), and (f) are 1.6 mm × 1.6 mm, while those shown in (c) and (e) are 6 mm × 6 mm. The fundamental and anharmonic wavelengths of the black eyes shown in (b) are 0.086 mm and 0.15 mm, respectively.

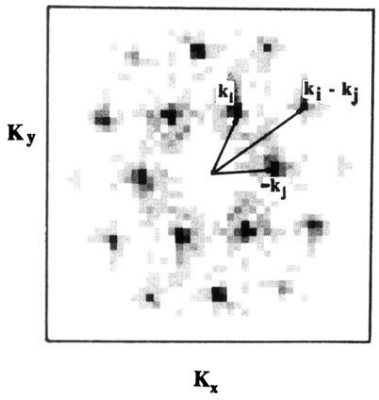

FIG. 9. Two-dimensional spatial Fourier transform of Fig. 8(b), showing the harmonic wave vectors that are responsible for the black-eye patterns.